Geosci. Model Dev. Discuss., 7, 3013–3084, 2014
www.geosci-model-dev-discuss.net/7/3013/2014/
doi:10.5194/gmdd-7-3013-2014

Geoscientific Model Development Discussions
Open Access

The coupled atmosphere-chemistry-ocean model SOCOL-MPIOM

S. Muthers[1,2], J. G. Anet[3], A. Stenke[3], C. C. Raible[1,2], E. Rozanov[3,4], S. Brönnimann[2,5], T. Peter[3], F. X. Arfeuille[2,5], A. I. Shapiro[4], J. Beer[6], F. Steinhilber[6], Y. Brugnara[2,5], and W. Schmutz[4]

[1]Climate and Environmental Physics, University of Bern, Bern, Switzerland
[2]Oeschger Centre for Climate Change Research, University of Bern, Bern, Switzerland
[3]Institute for Atmospheric and Climate Science, ETH, Zurich, Switzerland
[4]Physikalisch-Meteorologisches Observatorium Davos and World Radiation Center (PMOD/WRC), Davos, Switzerland
[5]Institute of Geography, University of Bern, Bern, Switzerland
[6]Swiss Federal Institute of Aquatic Science and Technology, Dübendorf, Switzerland

Received: 19 March 2014 – Accepted: 25 April 2014 – Published: 6 May 2014

Correspondence to: S. Muthers (muthers@climate.unibe.ch)

Published by Copernicus Publications on behalf of the European Geosciences Union.

Abstract

The newly developed atmosphere–ocean-chemistry-climate model SOCOL-MPIOM is presented by demonstrating the influence of the interactive chemistry module on the climate state and the variability. Therefore, we compare pre-industrial control simulations with (CHEM) and without (NOCHEM) interactive chemistry. In general, the influence of the chemistry on the mean state and the variability is small and mainly restricted to the stratosphere and mesosphere. The largest differences are found for the atmospheric dynamics in the polar regions, with slightly stronger northern and southern winter polar vortices in CHEM. The strengthening of the vortex is related to larger stratospheric temperature gradients, which are attributed to a parametrization of the absorption of ozone and oxygen in the Lyman-alpha, Schumann–Runge, Hartley, and Higgins bands. This effect is parametrized in the version with interactive chemistry only. A second reason for the temperature differences between CHEM and NOCHEM is related to diurnal variations in the ozone concentrations in the higher atmosphere, which are missing in NOCHEM. Furthermore, stratospheric water vapour concentrations differ substantially between the two experiments, but their effect on the temperatures is small. In both setups, the simulated intensity and variability of the northern polar vortex is inside the range of present day observations. Sudden stratospheric warming events are well reproduced in terms of their frequency, but the distribution amongst the winter months is too uniform.

Additionally, the performance of SOCOL-MPIOM under changing external forcings is assessed for the period 1600–2000 using an ensemble of simulations driven by a spectral solar forcing reconstruction. The amplitude of the reconstruction is large in comparison to other state-of-the-art reconstructions, providing an upper limit for the importance of the solar signal. In the pre-industrial period (1600–1850) the simulated surface temperature trends are in reasonable agreement with temperature reconstructions, although the multi-decadal variability is more pronounced. This enhanced variability can be attributed to the variability in the solar forcing. The simulated temperature reductions

GMDD
7, 3013–3084, 2014

during the Maunder Minimum are in the lowest probability range of the proxy records. During the Dalton Minimum, when also volcanic forcing is an important driver of temperature variations, the agreement is better. In the industrial period from 1850 onward SOCOL-MPIOM overestimates the temperature increase in comparison to observational data sets. Sensitivity simulations show that this overestimation can be attributed to the increasing trend in the solar forcing reconstruction that is used in this study and an additional warming induced by the simulated ozone changes.

1 Introduction

In recent years, the stratosphere has become more and more important for our understanding and proper simulation of climate variability and climate change (Baldwin et al., 2007; Gerber et al., 2012). While most of the CMIP3 models include only a poorly resolved stratosphere (Cordero and Forster, 2006), 14 of 39 general circulation models (GCMs) participating in CMIP5 include a "high-top" atmosphere, with a fully resolved stratosphere (Flato et al., 2013). The importance of the vertical resolution in the stratosphere is highlighted in several studies (Gillett et al., 2002; Sigmond et al., 2004; Scaife et al., 2011; Hardiman et al., 2012).

The stratosphere interact with the troposphere and plays an important role for the climate in the troposphere, at the surface and for the oceanic circulation (e.g. Baldwin and Dunkerton, 1999; Graversen and Christiansen, 2003; Thompson et al., 2005; Reichler et al., 2012). Furthermore, surface climate is influenced by changes in the chemical composition of the stratosphere (Gillett and Thompson, 2003; Son et al., 2010; Thompson et al., 2011). The interactions between stratosphere and troposphere are most prominent in the northern and southern high latitudes during winter time. With the beginning of the polar night stratospheric temperatures start to decrease rapidly and the increasing equator-pole temperature gradient forces a strong and persistent zonal circulation. This polar vortex isolates the polar air masses and prevents the advection of warmer air towards the polar latitudes. Very strong wind anomalies in the polar vortices

GMDD
7, 3013–3084, 2014

influence the circulation in the troposphere (Baldwin et al., 1994; Baldwin and Dunkerton, 2001; Thompson et al., 2005), a phenomena named stratosphere–troposphere coupling. Of particular relevance are unusually weak stratospheric zonal winds associated with a break down of the vortex (e.g., sudden stratospheric warmings). These disturbances are triggered by unusual wave activity propagating upward from the troposphere. Several processes were proposed to be involved in the wave propagation and to influence the stratosphere–troposphere coupling (Song and Robinson, 2004; Gerber et al., 2012), but the underlying mechanisms are still debated (Thompson et al., 2006; Gerber et al., 2012).

The winter climate at high latitudes is also closely related to the most important modes of variability, the Northern Annual Mode (NAM) in the Northern Hemisphere (NH) and the Southern Annual Mode (SAM) in the Southern Hemisphere (SH). These modes are found at any atmospheric level, from the stratosphere down to the surface. In the stratosphere, the NAM/SAM can be expressed by the variability of the polar vortices. At the surface the NAM is better known as the Arctic Oscillation (AO), which is basically the same phenomenon, though defined slightly differently, as the North Atlantic Oscillation (NAO) (Hurrell, 1995; Wanner et al., 2001; Pinto and Raible, 2012). The dynamical imprint of both is a North–South shift in the position of the maximum winds or jets in the troposphere. Stratosphere–troposphere coupling events connect these stratospheric and tropospheric modes of variability, hence a stronger polar vortex co-varies with a positive phase of the AO. Via the jet streams and their influence on tropospheric dynamics, the AO causally relates to, and thus is partially predictive of, weather patterns, with a negative AO index tending to be representative of high pressure in the polar region, weaker zonal winds, and greater movement of cold polar air into the mid latitudes.

These modes of variability are influenced by different external forcings, like changes in solar ultra-violet (UV) radiation (Haigh, 1994, 1996; Shindell et al., 1999; Kodera and Kuroda, 2002; Haigh et al., 2005; Labitzke, 2007; Anet et al., 2013b; Gray et al., 2013), volcanic aerosols (Graf et al., 1993; Stenchikov et al., 2002; Shindell et al., 2003;

GMDD
7, 3013–3084, 2014

Muthers et al., 2014), or ozone variations (Haigh, 1994; Shindell et al., 1999; Gillett and Thompson, 2003; Son et al., 2010; Kang et al., 2011; Thompson et al., 2011). Furthermore, NAM and SAM may interact with other modes of variability like the QBO or ENSO (Labitzke, 1987; Giorgetta et al., 1999; Labitzke, 2007). A common feature of these studies is a top-down perspective (e.g., Meehl et al., 2009) where a perturbation changes the vertical and horizontal temperature gradient in the stratosphere and affects stratospheric dynamics. The changing stratospheric wind systems alter the vertical propagation of planetary waves and change the circulation in the troposphere (Kodera, 1994; Kodera and Kuroda, 2002).

Differently, in the bottom-up mechanism the influence of an external forcing mainly takes place at the surface, e.g., the cooling after strong volcanic eruptions or variations in the surface temperatures related to variations in the solar forcing. Changes in the circulation and the climate are then modulated from the bottom of the atmosphere. Air-sea interactions may amplify the response (Meehl et al., 2008). This, however, does not mean that the stratosphere is not involved. Stenchikov et al. (2002) found for the effect of volcanic aerosols that a change at the bottom also influences the stratospheric circulation. They found a change in the vertical component of the Eliassen–Palm flux, a vector determining the relative importance of the eddy heat and momentum fluxes for the propagation of waves, which indicates a reduction of the wave drag in the lower stratosphere. Climate model results further suggest that both, top-down and the bottom-up mechanisms, need to act together to produce a realistic response similar to the observations (Meehl et al., 2009).

The dynamics in the stratosphere interacts also with a large number of chemical processes, most important the ozone chemistry (Haigh, 1994; Shindell et al., 1999, 2001; Gillett and Thompson, 2003; Son et al., 2010; Thompson et al., 2011; Purich and Son, 2012; Varma et al., 2012). In case of the solar forcing, the variability in the UV part of the spectrum modulates the ozone production and heating rates followed by positive or negative temperature anomalies. These anomalies influence the equator-to-pole gradient, the strength of the polar vortices, and modify the Brewer–Dobson circulation

GMDD
7, 3013–3084, 2014

(Haigh, 1994; Hu and Tung, 2003; Anet et al., 2013a). In case of volcanic aerosols, heterogeneous reactions take place on the aerosol surface, which also influence the ozone chemistry (Tie and Brasseur, 1995; Solomon et al., 1996; Anet et al., 2013a). In both cases, the response of the ozone chemistry is further modulated by the presence of ozone depleting halogens (Tie and Brasseur, 1995; Rozanov et al., 2002). The changing ozone concentrations in turn induce dynamical changes (Stenchikov et al., 2002).

Coupled climate models have been proven to be an essential tool for understanding processes and feedbacks between the different components of the climate system, e.g., between ocean and atmosphere. Chemistry transport models (CTMs) are numerical models that simulate a number of chemical species, their interactions and the influences of different atmospheric variables (temperature, shortwave and longwave flux, etc.). GCMs coupled to CTMs allow a direct consideration of chemistry–climate interactions. Most of the coupled chemistry–climate model (CCM) simulations so far were performed with prescribed sea surface temperatures (SSTs; e.g., Eyring et al., 2006) or simplified mixed-layer oceans (e.g., Stenke et al., 2013a). However, imposed SSTs can alter the stratosphere–troposphere interaction (Kirchner et al., 1999). The coupling to an interactive ocean model is therefore preferable for long-term simulations and future projections.

The purpose of this study is to present the atmosphere–ocean-chemistry-climate model (AOCCM) SOCOL-MPIOM. The atmospheric component of the model covers the atmosphere from the surface to the mesosphere (0.01 hPa) and enables the simulation of interactions between the physical and the chemical components of the climate system. In Sect. 2 the model is introduced and an overview of the experiments used in this study is given. In Sect. 3 the performance and the characteristic of the AOCCM SOCOL-MPIOM are evaluated using results from a pre-industrial control simulation. The effect of the atmospheric chemistry on the climate is assessed by comparing it to a simulation without interactive chemistry. Furthermore, we describe an ensemble of transient simulations for the period 1600–2000 to assess the behaviour of

GMDD
7, 3013–3084, 2014

SOCOL-MPIOM under the influence of changing external forcings (Sect. 4). Finally, we close with a discussion and a summary of the results.

2 Model description and experimental setup

2.1 Model description

The coupled model consists of the chemistry-climate model SOCOL (SOlar Climate Ozone Links), which is coupled to the ocean–sea-ice model MPIOM by the OASIS3 coupler. The CCM SOCOL version 3 (Stenke et al., 2013b) is based on the middle atmosphere model MA-ECHAM5 version 5.4.01 (Roeckner et al., 2003) and a modified version of the chemistry model MEZON (Model for Evaluation of oZONe trends, Rozanov et al., 1999, 2001; Egorova et al., 2003; Hoyle, 2005; Schraner et al., 2008).

MA-ECHAM5: this is a spectral general circulation model (GCM) based on the primitive equations with temperature, vorticity, divergence, the surface pressure, humidity, and cloud water as prognostic variables (Roeckner et al., 2003, 2006; Manzini et al., 2006). In the vertical dimension a hybrid sigma-pressure coordinate system is used.

The shortwave (SW) radiation code originates from the European Centre of Medium-Range Weather Forecasts (ECMWF) model IFS (Fouquart and Bonnel, 1980). The solar spectrum is split into six wavelength intervals, including three bands in the UV and visible ranges (185–250 nm, 250–440 nm, 440–690 nm) and three bands in the near-IR range (690–1190 nm, 1190–2380 nm, 2380–4000 nm) (Cagnazzo et al., 2007). This SW scheme considers Rayleigh scattering, scattering and absorption by aerosols and clouds, and the absorption of solar irradiance by water vapour, ozone (both varying in space and time) as well as CO_2, N_2O, CH_4, and O_2. The latter are considered as uniformly mixed gases in MA-ECHAM5, but CH_4 and N_2O can optionally also vary in time and space (as it is done in SOCOL).

The longwave (LW) radiation scheme follows the rapid radiative transfer model (RRTM) scheme (Mlawer et al., 1997), which calculates radiation fluxes and heating

GMDD
7, 3013–3084, 2014

rates over 16 LW bands reaching from 10–3000 cm^{-1}. In the computations absorption by water vapour, CO_2, ozone, N_2O, CH_4, CFC-11, CFC-12, CFC-22, aerosols, as well as clouds are considered.

With the vertical resolution used in this study (39 levels up to 0.01 hPa), the model does not produce a Quasi-Biennial Oscillation (QBO) by itself. Therefore, a QBO nudging is applied by a linear relaxation of the zonal winds in the equatorial stratosphere (Giorgetta et al., 1999). The model assimilates the input data between 20° N to 20° S in the horizontal and from 90 hPa up to 3 hPa in the vertical. ECHAM5 also includes a river run-off scheme (Hagemann and Duemenil, 1998; Hagemann and Duemenil-Gates, 2003) and simplified glacier calving, in the way that snow falling on ice sheets is instantaneously transferred to the next ocean grid cell.

Chemistry-climate coupling: MEZON and MA-ECHAM5 are coupled by the three dimensional temperature field and the radiative forcing of the different greenhouse gases (H_2O, O_3, CH_4, N_2O, and CFCs).

SOCOL: in the chemical module, 31 chemical species can react together via 140 gas-phase-, 46 photolysis-, and 16 heterogeneous reactions. The latter appear either in or on aqueous sulphuric acid aerosols as well as on three types of Polar Stratospheric Clouds (PSCs), i.e., on supercooled ternary solution (STS) droplets, water ice, or nitric acid trihydrate (NAT).

For SOCOL, the SW radiation code of MA-ECHAM5 has been modified in several aspects. In MA-ECHAM5 variations in the solar forcing are considered by variations in the total solar irradiance (TSI), the ratio of the irradiance in the six SW bands to the TSI, however, is fixed. SOCOL directly uses the spectral solar irradiance (SSI) as input for the six bands and, therefore, allows for a change in the spectral composition. As the absorption of radiation by oxygen and ozone in the Lyman-alpha, Schumann–Runge, Hartley, and Higgins bands is only partially included in MA-ECHAM5, missing heating rates are parametrized using an approach similar to Egorova et al. (2004).

The time step for the dynamical processes and physical parametrizations in the model is 15 min with a spectral truncation of T31. However, to reduce the high

GMDD
7, 3013–3084, 2014

computational demand of the chemistry module, the chemical routines are called – simultaneously to the full radiative transfer calculations – every two hours. Over the two hour interval the heating rates are estimated based on the 2 hourly radiative transfer calculations and the solar angle that is calculated at every time step.

Precipitation of energetic particles into the atmosphere is simulated by different parametrizations for galactic cosmic rays (GCR), low energetic electrons (LEE) and solar energetic proton (SEP) events (Calisto et al., 2011; Rozanov et al., 2012). The routines are designed in such a way that from the known ionization rate distributions, a certain amount of N (GCR, SPE, LEE), NO (GCR, SPE, LEE) and OH (GCR, SPE) is produced.

Additionally to the interactive chemistry mode the chemistry module can be deactivated. In this case prescribed three dimensional ozone concentrations are used for the radiative transfer calculations. These ozone concentrations can origin from a model simulation with interactive chemistry. By forcing the model with ozone concentrations directly on the model grid, errors related to the vertical interpolation can be avoided. In contrast to many other models, SOCOL does not use zonally averaged ozone concentrations, as this leads to significant biases in the stratospheric climate and also affects tropospheric dynamics (Waugh et al., 2009). Zonally averaged ozone forcing also might influence the propagation of planetary waves (Gabriel et al., 2007). In the setup without interactive chemistry the model version is nearly identical to MA-ECHAM5, except for the modification related to the SSI forcing mentioned above. Furthermore, the additional heating by absorption in the Lyman-alpha, Schumann–Runge, Hartley, and Higgins band is by default deactivated. Despite the small differences to MA-ECHAM5, these modifications lead to a significant change in the simulated climate.

MPIOM: the oceanic component consists of the ocean model MPIOM (Marsland, 2003; Jungclaus et al., 2006) including a sea-ice component. It uses an Arakawa C grid with the North Pole shifted to Greenland and the South Pole centred over Antarctica. Shifting the poles towards land surfaces avoids numerical singularities at the North Pole and allows a higher resolution in the deep water formation regions in the North Atlantic.

GMDD
7, 3013–3084, 2014

The grid has a nominal resolution of 3°, that varies between 22 km near Greenland and 350 km in the tropical Pacific. In the vertical the grid is divided into 40 levels with decreasing resolution from the surface to the bottom. The time step of the calculations in the ocean model is 144 min in this setup.

Atmosphere–ocean coupling: both components, the atmosphere and the ocean, are coupled every 24 h using the OASIS3 coupler (Budich et al., 2010; Valcke, 2013). For each day the coupler transfers momentum, heat, and freshwater fluxes from the atmosphere to the ocean and sea surface temperatures (SST), sea ice, snow cover on sea ice, and momentum to the atmosphere. No flux correction is needed in the coupling process.

2.2 Experiments

To assess the influence of the interactive chemistry on the climate state a 1400 year long 1600 AD control simulation with interactive chemistry (CHEM) is compared to a simulation under the same set of boundary conditions, but without interactive chemistry (NOCHEM). Furthermore, an ensemble of transient simulations, i.e., with varying boundary conditions, covering the period 1600–2000 AD is performed. An overview of the experiments used in this study is given in Table 1.

2.2.1 Control simulations

For the control experiment, SOCOL uses a horizontal resolution of T31 (approx. 3.75° × 3.75°) and 39 vertical levels, resolving the atmosphere up to 0.01 hPa (approx. 80 km). The ocean component is branched of from the initial conditions of a transient millennium simulation with the MPI–ESM (ECHAM5–MPIOM with additional models for the land and ocean carbon cycle) for the year 1600 AD (Jungclaus et al., 2010). The atmospheric and chemistry components are initialized from scratch.

The control simulation is performed as time-slice experiment and all forcings are held constant at 1600 AD conditions (CO_2: 276.4 ppm, CH_4: 692.7 ppb, N_2O: 269.0 ppb),

GMDD
7, 3013–3084, 2014

except for the volcanic aerosol forcing, where the unperturbed year 1599 is chosen. For the land-surface boundary condition the forcing from the ECHAM5 package is used, representing present day values (Hagemann, 2002). The QBO-nudging uses an idealized QBO cycle based on Brönnimann et al. (2007), to avoid an unrealistic dominance of a westerly or easterly QBO phase.

The oceanic component of SOCOL-MPIOM is initialized using restart files from the coupled system ECHAM5–MPIOM. However, when assuming a total solar irradiance (TSI) of 1367 $W m^{-2}$ (as in ECHAM5–MPIOM) the new SOCOL-MPIOM experiences a positive temperature drift that requires a tuning of the model. As tuning parameter the value of the TSI is chosen. To estimate the optimal tuning value for the TSI, a number of 200 year experiments with constant TSI reductions chosen between from 0 $W m^{-2}$ to -18 $W m^{-2}$ relative to the 1368 $W m^{-2}$ reference value is performed. All experiment are forced by constant 1600 AD boundary conditions and started from the same initial state. The simulations with the smallest temperature drift is continued for another 1200 years and used as control simulation in this publication. It is forced by a solar constant of 1355 $W m^{-2}$. This value is meant to represent 1600 conditions. With the solar forcing reconstruction of Shapiro et al. (2011), which is used in the transient simulations (see below), this corresponds to a TSI of 1358.7 $W m^{-2}$ for the year 1990. The new TSI value used for SOCOL-MPIOM therefore agrees reasonably well with the most recent TSI estimate of 1360.8 ± 0.5 $W m^{-2}$ (Kopp and Lean, 2011).

To assess the influence of the chemistry module on the climate state and variability a second control experiment without interactive chemistry is performed (NOCHEM). This simulation is branched off 1178 years after the start of the interactive simulation. The length of this experiment is 222 years. Both simulations are driven by the same forcings and boundary conditions, except for the forcings specific for the chemistry module, which are not considered in NOCHEM. Furthermore, ozone values need to be prescribed in NOCHEM in order to consider the effect of ozone in the radiation scheme. Here, a 4 dimensional, daily ozone climatology calculated over the simulation years 1178 to 1399 (length 222 years) of CHEM is used.

GMDD
7, 3013–3084, 2014

The control simulations are needed to (a) assess a potential underlying temperature drift due to the coupling of the model components, (b) as initial conditions for the transient simulations, and (c) to characterize the role of the interactive chemistry module on the climate. Due to the high computational demand of the chemistry computations and the slow adjustment time of the ocean it was not possible to perform a second control simulation for 1990 conditions, as it is usually done in model evaluation studies.

2.2.2 Climate sensitivity experiments

The climate sensitivity of SOCOL-MPIOM is analysed by two types of experiments (Table 1).

The transient climate response (TCR) is estimated using an experiment with 1 % yr^{-1} CO_2 increase until a doubling of the CO_2 concentrations is reached (Cubasch et al., 2001). The TCR is then defined by the global mean temperature change in the 20 yr period around the year of the doubling of the CO_2 concentrations.

Furthermore, we estimate the equilibrium response of the model following the approach by Gregory et al. (2004). Therefore, the coupled model is forced by an instantaneous quadrupling of the CO_2 concentrations and the equilibrium climate sensitivity (ECS) is estimated based on a linear relationship between the TOA radiative flux and the global mean surface air temperature after a simulation length of 150 years.

Both experiments are initialized using 1990 conditions from the transient simulation M1. All other forcings are constant at 1990 level. The underlying positive temperature drift is assessed by a reference simulation without changing CO_2 concentrations. The temperature increase is then calculated relative to this experiment.

Finally, the influence on the interactive chemistry on the TCR is analysed using a second TCR experiment, where the chemistry module is disabled. The ozone climatology for this simulation is based in the simulated ozone in the 1990 reference experiment.

GMDD
7, 3013–3084, 2014

2.2.3 Transient simulations

A set of four transient simulations for the period 1600–2000 AD is started from initial conditions of the CHEM control simulation using SOCOL-MPIOM with interactive chemistry. An overview of the external forcings is given in Fig. 1. Greenhouse gas (GHG) forcings (CO_2, CH_4, and N_2O) are taken from the PMIP3 database (Etheridge et al., 1996, 1998; MacFarling-Meure, 2004; Ferretti et al., 2005; MacFarling-Meure et al., 2006). Emissions of ozone depleting substances (ODS) are based on the historical concentrations from the CMIP5 database.

For the solar forcing reconstructed spectral solar irradiance (SSI) values from Shapiro et al. (2011) are used, which are shown as total solar irradiance (TSI) in Fig. 1. The reconstruction of Shapiro et al. (2011) is based on the solar modulation potential derived from ^{10}Be measurements in polar ice cores. In comparison to many other state-of-the-art solar forcing reconstructions, this reconstruction is characterized by a larger amplitude (Schmidt et al., 2012). The TSI difference between the Maunder Minimum (end of the 17 century) and present day is in the order of $6 \pm 3\,W\,m^{-2}$. To consider larger and smaller variations, we created two SSI datasets both covering the uncertainty range of the reconstruction. The larger amplitude forcing represents the mean estimate of $6\,W\,m^{-2}$ (dashed line in Fig. 1), the second forcing with $3\,W\,m^{-2}$ amplitude (solid line) represents the upper boundary of the uncertainty of the SSI reconstruction. The two solar forcing scenarios will be referred to as L (large) and M (medium) in the following. Note that compared to other recent estimates a TSI difference of $3\,W\,m^{-2}$ between Maunder Minimum and present day is still considered to be large. In Steinhilber et al. (2009) for example the forcing difference between Maunder Minimum (MM) and present day is only $0.9 \pm 0.4\,W\,m^{-2}$.

The SW radiation scheme in SOCOL has been modified in comparison to the original scheme distributed with ECHAM5. In the original ECHAM5 the SW spectra is divided into 6 spectral intervals and the TSI is distributed over the six spectral bands using fixed ratios. In the SW scheme of SOCOL the solar energy input can be prescribed for each

GMDD
7, 3013–3084, 2014

band individually. This allows for a different variability in different spectral intervals. The differences in the spectral partitioning between SOCOL and ECHAM5 are pronounced, when the spectral solar reconstruction of Shapiro et al. (2011) is used (Fig. 1 b). In the UV region (< 440 nm), considerably less energy is available in SOCOL (differences > 6 $W m^{-2}$ in UV2), but the multi-decadal scale variability is larger. Between the Maunder Minimum and the following period of high solar activity around 1780, the differences reach up to 6 $W m^{-2}$. In the visible band (440–690 nm) a higher energy input is assumed in SOCOL, which explains the positive temperature bias in SOCOL-MPIOM compared to the ECHAM5–MPIOM that required the tuning of the model (see above). Differences in this spectral interval are in the order of 15 $W m^{-2}$. Between 690–1190 nm and 2380–4000 nm, the energy input is again larger in ECHAM5 (+5.5 $W m^{-2}$ and +4.5 $W m^{-2}$, respectively), for the interval 1190–2380 nm larger SSI values are found in SOCOL (+3.5 $W m^{-2}$).

Other solar related forcings, like photolysis rates for the chemistry or the input for the parametrizations of the additional heating by oxygen or ozone absorption, are generated based on the SSI data set.

Four experiments are performed with two sharing the same solar forcing. We refer to the experiments as L1 and L2 for the large amplitude solar forcing and M1 and M2 for the medium amplitude solar forcing in the following. All other forcings are identical in the four simulations. The experiment M1 and M2 are initialized using restart files for the ocean and the atmosphere from the CHEM simulation (model year 450 and 500). To produce the initial conditions for L1 and L2 a second control simulation is performed. This experiment is identical to CHEM, with the only difference of an lower solar forcing, which is reduced by the forcing difference between the medium and the large amplitude solar forcing for the year 1600 (Fig. 1). From this control simulation, the restart files are also extracted for model year 450 and 500.

The stratospheric aerosols (Fig. 1) used in the simulations are described in Arfeuille et al. (2014). Aerosol optical properties (spectrally dependent) for the radiation scheme and surface area density information for the chemistry scheme are calculated offline

GMDD
7, 3013–3084, 2014

using a microphysical aerosol model AER (Weisenstein et al., 1997) and stratospheric aerosol mass information from ice cores (Gao et al., 2008).

Tropospheric aerosols are based on CAM3.5 simulations with a bulk aerosol model driven by fixed SSTs and the 1850–2000 CMIP5 emissions (S. Bauer, personal communication, 2011). Before 1850, the aerosol concentrations are scaled by the world population except for 10 % of the presumed 1990 biomass burning aerosols which are considered natural.

The emissions of CO and NO_x are based on the historical CMIP5 data sets which are available from 1850 onwards. Before 1850 the anthropogenic fraction is scaled linearly with world population. The biomass burning emissions are assumed to be constant over time. Emissions from shipping are projected linearly back to 1800, before 1800 the emissions are set to zero.

The lower boundary condition over land (land surface data) is kept at present day values as in the control simulation (Hagemann, 2002). For the QBO nudging, the QBO reconstruction from Brönnimann et al. (2007) is included, which is extended back in time to cover the full period 1600–2000. For this backward extension an idealized QBO cycle and annual cycle is assumed.

The cosmic ray intensity is reconstructed based on the solar modulation potential (Steinhilber et al., 2008). Available observations for solar proton events (SPE) are used for the periods 1963–2008 (Jackman et al., 2009). Before 1963 SPEs are randomized using a return-period based analysis of the last 45 yr, and weighted with the Ap index, an index of the geomagnetic activity. The NO_x influx, finally, is reconstructed based on the Ap and the Aa index, which are themselves reconstructed using sunspot numbers (Baumgaertner et al., 2009). Paleo-magnetic datasets (C. Finlay, personal communication, 2010) are applied to the model in order to take into account the geomagnetic dependency of the ionization.

In the analysis all transient simulations are detrended by subtracting the underlying positive trend estimated from the control simulation.

GMDD
7, 3013–3084, 2014

2.2.4 Sensitivity simulations

The contributions from different external forcings to the temperature increase from 1850 to 2000 is assessed by a set of sensitivity experiments (Table 1). In these simulations specific forcings are held either constant at pre-industrial levels or prescribed in a transient way. All simulations are initialized in the year 1840 using the atmospheric state of the transient simulation M1.

For these sensitivity experiments, the version of SOCOL-MPIOM without interactive chemistry is used. This setup allows us to use fixed ozone concentrations at pre-industrial levels or to prescribe the simulated ozone from the transient simulations as forcing. In this way the radiative effect of the simulated ozone changes can be assessed. The following forcings are considered:

- SOLAR: solar forcing with medium amplitude. In this experiment the increase in TSI since 1900 is 1.7 $W m^{-2}$ (TOA).
- GHG: For this experiment only the major GHGs (CO_2, CH_4, and N_2O) increase (see Fig. 1 a), except for CFCs.
- AERO: Only stratospheric and tropospheric aerosols change.

For these three experiments ozone concentrations are held constant at pre-industrial levels.

- OZONE: In this experiment only ozone is used as time varying forcing. The ozone concentrations used as forcing are extracted from M1, but the concentrations in the other three transient experiments are very similar.
- FULL: All major forcings (solar, GHGs, aerosols, ozone) are included in this simulation.

For each forcing combination a single experiment is performed. The forcing from CFCs are not considered in the sensitivity experiments.

GMDD
7, 3013–3084, 2014

2.3 Observational data sets

To evaluate the simulated climate variables different observational data sets are used throughout this study.

The stratospheric temperatures and dynamics in the control simulation are compared to the two reanalysis products ERA40 (Uppala et al., 2005) and ERA Interim (Dee et al., 2011) from the European Centre for Medium Range Weather Forecasts (ECMWF). ERA40 covers the period 1957–2002, while for ERA Interim the years 1979–2013 are considered.

The simulated temperature increase since the second half of the 19 century is compared to two global surface air temperature data sets and a reanalysis product. The Goddard Institute for Space Studies Surface Temperature analysis (GISTEMP) contains a spatial land and ocean surface temperature analysis for the period 1880–2013 (Hansen et al., 2010). The data set is solely based on instrumental records from meteorological stations, ships, buoys, and other. The data from land stations are corrected for urban heat island effects using satellite observations. SSTs are based on the NOAA data set ERSST (Smith et al., 2008). The second temperature data set is from the Climatic Research Unit at the Hadley Centre of the UK Met Office (HadCRUT4). It is also based on instrumental temperature records and covers the period 1850–2013 (Brohan et al., 2006). HadCRUT4 makes use of the SST data set HadSST3 for the conditions over oceans (Kennedy et al., 2011).

Additionally, we use the 20 century reanalysis (20CR; Compo et al., 2011). By assimilating only sea level pressure, SST and sea ice informations (HadISST; Rayner et al., 2003) as boundary conditions, 20CR generates a physically consistent, three dimensional picture of the atmosphere with high temporal resolution. 20CR contains 56 ensemble members, to consider uncertainties in the boundary conditions. The reanalysis covers the period 1871–2010.

GMDD
7, 3013–3084, 2014

3 Pre-industrial model climatology and imprint of atmospheric chemistry

In this section, the mean climate state and the most important variability patterns in a pre-industrial (1600 AD) control simulation of SOCOL-MPIOM is described and the difference between a simulation including interactive chemistry (CHEM) and a simulation without interactive chemistry (NOCHEM) is analysed.

The development of the global mean 2 m air temperature in the control simulation CHEM is shown in Fig. 2. Despite the tuning approach described above, the simulation is still dominated by a continuous positive drift of 0.037 °C/100 yr, averaged over the last 500 simulation years. The temperature trend is slightly larger in the SH (0.038 °C/100 yr) than in the NH (0.036 °C/100 yr) and stronger over land than over the ocean.

For the last 500 years, the largest positive temperatures trends are found in the polar regions, especially in the Barents and the Weddell Seas (Fig. 2). Here, the overall positive drift affects the sea ice edge, which amplifies the temperature trends. Clearly, the warming of the atmosphere near the surface influences also the state of ocean. On all levels, down to the deep ocean a positive temperature trend is present, reaching, e.g., 0.05 °C/100 yr at depth around 3500 m.

In the common 222 yr period the global mean 2 m air temperature in CHEM and NOCHEM is very similar, besides some variations related to the model's internal variability (Fig. 2c and d). This confirms that the interactive chemistry does not affect the model equilibrium. Furthermore, the drift in the 2 m temperatures is no longer significant in this 222 yr period. Still, the oceanic temperatures are not in equilibrium.

With an average value of 14.45 °C for CHEM the simulated global mean temperature is higher than the pre-industrial observed mean over 1850–1890 of 13.7 ± 0.2 °C (Brohan et al., 2006). However, the value is similar to the global mean temperature in the MPI-ESM based on ECHAM5 and MPIOM (Fig. 4 in Mauritsen et al., 2012). From the ongoing temperature drift it can be assumed that the model has not reached equilibrium so far. The top-of-the-atmosphere (TOA) radiation balance is still characterized

GMDD
7, 3013–3084, 2014

by a positive imbalance of 1.6 $W m^{-2}$, averaged over the last 100 years of the simulations. However, most climate models do not exactly conserve energy (Mauritsen et al., 2012). Nevertheless, compared to the MPI-ESM, which has an imbalance of approximately 1 $W m^{-2}$, the temperatures are likely to adjust further, even after 1400 years of simulation.

In the following the differences in the mean climate and the variability between CHEM and NOCHEM for different variables and components of the climate system is presented.

3.1 Stratospheric changes with interactive chemistry

3.1.1 Ozone variability

A detailed evaluation of the chemistry in SOCOL3 is given in Stenke et al. (2013b). Here, we focus only on the simulated variability in stratospheric ozone concentrations and their possible influence on the climate variability. The main difference between CHEM and NOCHEM is the fact that ozone concentrations vary on all time scales in CHEM, whereas NOCHEM is driven by an ozone climatology, which represents the climatological annual cycle and therefore does not contain any variability on time scales shorter than one day and longer than one year.

The time series of global mean ozone mixing ratios at different pressure altitudes reveal that variability takes place on different time-scales, from day-to-day up to the decadal scale. A pronounced and significant 2.3 yr periodicity is found, which is the QBO imprint on the ozone chemistry.

In the zonal mean perspective the largest variability is found in the tropics at the altitude of the concentration maximum (Fig. 3). Secondary maxima occur in the lower stratosphere in both polar regions. The normalized variability (Fig. 3) is more pronounced in the polar stratosphere of both hemispheres compared to the tropics. Variability in the troposphere and mesosphere is in general very small and is only reflected in the normalized anomalies. The variations are more pronounced on the

GMDD
7, 3013–3084, 2014

intra-seasonal scale (not shown), where for the NH polar stratosphere, the variability in the winter season (DJF) ozone concentrations exceeds 10 %. The variability in the vertically integrated total column ozone reflects the pattern found for the zonal averages (not shown). The northern and southern polar regions are characterized by the highest interannual variability, while the variability in the north is larger than in the south. In the Arctic, variability is particularly pronounced in the boreal winter and spring season. Over Antarctica, larger variances are found mainly during austral spring.

3.1.2 Temperatures

The seasonal zonal mean differences in the air temperature between CHEM and NOCHEM are presented in Fig. 4a.

The largest temperature differences are found in the mesosphere, where CHEM is more than 3 °C warmer. These differences are most pronounced in the summer season of the corresponding hemisphere. In the upper and middle stratosphere the temperatures are significantly higher at latitudes between 30° and 50° on both hemispheres and significantly lower in polar regions. The positive differences are below 0.6 °C and do not show a clear seasonal variation. The negative differences in the lower stratosphere are most pronounced and significant during winter and spring and reach up to −1.5 °C.

The higher mesospheric and upper stratospheric temperatures in CHEM are result of different processes. In SOCOL-MPIOM with interactive chemistry a parametrization of the absorption of radiation by oxygen and ozone in the Lyman-alpha, Schumann–Runge, Hartley, and Higgins bands is included. This effect creates additional heating in the higher atmosphere, which is not included in NOCHEM. Tests show that this parametrization is responsible for a pronounced heating of the higher atmosphere, especially in summer. In the annual average the temperature is up to 7 °C warmer and the effect is visible at all latitudes in the mesosphere and upper stratosphere. Therefore, an additional negative signal in the mesosphere is needed to create the pattern shown in Fig. 4.

GMDD
7, 3013–3084, 2014

One mechanism that is responsible for colder conditions in the higher atmosphere in the case of the setup with interactive chemistry is found in the interactions between the chemical module and the SW radiation scheme. In NOCHEM ozone concentrations are prescribed as a daily climatology, whereas ozone in CHEM varies from time step to time step. In the mesosphere ozone undergoes a pronounced diurnal cycle. During daytime ozone is destroyed by UV radiation and in the night the transport of ozone enriched air from lower levels leads to an increase in the ozone concentrations. Differences between night and day reach up to 15 %. Consequently, the highest model levels in CHEM are colder during daytime, but this cooling can not be compensated at night. The diurnal cycle of the ozone concentrations in the mesosphere has a cooling effect of around 5 °C, which is largest at 30° N and 30° S.

Additional differences between CHEM and NOCHEM are found in the water vapour concentrations (not shown). In the NOCHEM configuration the only source of water vapour in the stratosphere and mesosphere is the transport from the troposphere. With interactive chemistry water vapour is also produced by the oxidation of CH_4. Large differences in the specific humidity between NOCHEM and CHEM are found in the summer hemisphere and at altitudes above 40 km, where the values differ by up to 37 %. The higher water vapour mixing ratios in CHEM lead to a cooling of the higher atmosphere between 60° S and 60° N. In the annual mean the maximum anomalies are in the order of 1 °C. Contrary to Maycock et al. (2011) who reported a maximum cooling in the lower stratosphere after a uniform increase of the stratospheric water vapour, the cooling effect in SOCOL-MPIOM is strongest in the upper stratosphere and mesosphere. This is probably related to the fact that the water vapour difference between CHEM and NOCHEM are not uniformly distributed and reach the largest differences in the higher stratosphere.

Further tests for the parametrization of GCR, LEE, and SEP events show that these parametrizations does not substantially affect the atmospheric temperatures.

GMDD
7, 3013–3084, 2014

3.1.3 Dynamics

The differences in the zonal wind component reflect the changes in the meridional temperature gradients (Fig. 4b). Both polar vortices are significantly strengthened during winter and spring in the case of the simulation with interactive chemistry. With this vortex intensification, the colder conditions in CHEM in the SH and NH polar stratosphere can be understood: a stronger vortex isolates the air masses over the poles and prevents the meridional transport of warmer air into the vortex centre. Both differences, the temperature and the zonal wind speed, are larger in the SH. In the summer hemisphere, the changed temperature gradient forces a strengthening of the easterly circulation at mesospheric levels.

A comparison between model results and observations for the zonal wind component at 50 hPa in the boreal winter season is given in Table 2. Similar to Driscoll et al. (2012), we average over the tropical latitudes (30° S–30° N) and the northern mid latitudes (55° N–65° N) and compare to against the reanalysis products ERA40 and ERA Interim, covering the period 1957–2002 and 1979–2013, respectively.

In the tropical latitudes the average wind conditions and the standard deviation are lower compared to the values in ERA Interim. However, SOCOL-MPIOM agrees much better with ERA Interim than the CMIP5 models evaluated by Driscoll et al. (2012), which can be attributed to the QBO nudging implemented in the model. No significant difference is found between CHEM and NOCHEM for the tropical indices. For the northern polar night jet the difference between CHEM and NOCHEM becomes slightly larger, illustrated by stronger zonal wind in winter for CHEM. The differences are not very large ($0.6\,m\,s^{-1}$), but statistically significant. The variability in the daily mean zonal wind component does not differ significantly between CHEM and NOCHEM. Compared to ERA Interim SOCOL-MPIOM simulates higher zonal winds with a slightly lower standard deviation. Still, the agreement is better than in most CMIP5 models evaluated by Driscoll et al. (2012). In particular this agreement is notable, since earlier studies suggested that the underestimation of stratosphere–troposphere coupling events after

GMDD
7, 3013–3084, 2014

tropical volcanic eruptions may be related to a too strong and too stable northern polar vortex in many GCMs (Stenchikov et al., 2006; Driscoll et al., 2012). Although the different climate states, pre-industrial control vs. late 20 century, might bias the comparison there is confidence that SOCOL-MPIOM simulates wind conditions in the tropical and northern high latitudes reasonably well. Furthermore, the comparison between CHEM and NOCHEM reveals an influence of interactive ozone chemistry on the mean intensity of the winter northern polar vortex.

The stability of the northern polar vortex is closely related to sudden stratospheric warming events (SSW). Major SSWs are stratospheric extreme events, in which the westerly flow during winter time is reversed and a strong warming in the polar stratosphere can be observed. SSW events in the NH are associated with a "break down" of the polar vortex and are consequently also reflected in the NAM. Via stratosphere–troposphere interactions, SSW events influence the storm-track activity (Thompson and Wallace, 2001; Breiteig, 2008) and the increase of blocking situations (Woollings et al., 2010). Here we assess the ability of SOCOL-MPIOM in simulating of SSWs and possible influences of the interactive chemistry on the frequency of SSWs. Again, we use the two reanalysis products from the ECMWF and compare them to the values from the two pre-industrial control simulations. SSW events are based on the definition of Charlton and Polvani (2007). The central date of an event is defined as the day during the months November to March when the zonal mean wind component at 60° N and 10 hPa changes from westerly to easterly direction. The following 20 days after the onset of an event are excluded from the analysis to avoid double counting single events. Final warming events at the end of the winter season are excluded by an additional constraint demanding that the last events need to be followed by at least 10 days with westward wind conditions before the end of April.

The total number of SSW events per winter is similar to ERA 40 and ERA Interim (Table 3). During the winter months SOCOL-MPIOM simulates a too uniform distribution of SSWs. In the reanalysis a clear maximum is found in January (ERA 40) or February (ERA Interim), whereas both experiments simulate a minimum of events in January.

GMDD
7, 3013–3084, 2014

Note that the difference between ERA 40 and ERA Interim is due to the different periods, in the common period 1979–2002 the difference is negligible. With interactive chemistry less SSW events are simulated, which may be related to the stronger polar vortex in CHEM.

Note that this more realistic simulation of SSWs is a major improvement to earlier versions of SOCOL (Fischer et al., 2008) and is attributed to a better representation of the stratospheric temperatures in the polar regions in winter and spring (Stenke et al., 2013b).

In the NOCHEM simulation, the ozone forcing is implemented in terms of a four dimensional ozone climatology, representing the average annual cycle at each grid point. Any interannual variability in the ozone mixing ratios is excluded by this approach. This may affect different physical variables of the atmosphere and reduce their variability on interannual time scales.

Changes in the interannual variability of the zonal mean temperatures and zonal winds are described in the following. Therefore, the ratio of the two variances, i.e. $\frac{\mathrm{var(CHEM)}}{\mathrm{var(NOCHEM)}}$ is calculated. A ratio of 1 corresponds to no change, values < 1 (> 1) to a reduction (increase) of the variance with interactive chemistry. Results for the seasonal averages are shown in Fig. 4. The highest variability in the zonal wind is found in the tropical stratosphere for all seasons (contours). This pattern is related to the QBO. Secondary maxima of the variability are found in the NH during DJF and MAM, related to the winter polar vortex. In the SH the variability of the polar vortex is lower, i.e., the vortex is more stable in the winter months. Still, a second maxima is found for austral spring in the vortex region. In the NH, the variability in the winter vortex is enhanced in the southern part of the vortex and reduced in the centre of the vortex with interactive chemistry. A slightly lower variability in the centre may be related to the overall stronger vortex and is also reflected in the lower number of SSW events. The increasing variability in the mid-latitudes could be related to the chemistry, however, the differences are marginally significant. A significant increase in the variability in the northern polar vortex is found for the boreal spring season. In the SH, the low variability in the winter

GMDD
7, 3013–3084, 2014

polar vortex is slightly (albeit significantly) higher in winter, but reduced in the following spring season.

In summary, the largest differences between the simulation with and without interactive chemistry are only indirectly related to the chemistry. With interactive chemistry the absorption of oxygen and ozone in different wavelength bands leads to enhanced heating rates in the upper atmosphere. This warming is compensated by interactions between the diurnal cycle of mesospheric ozone and the SW radiation scheme. Furthermore, the stratospheric water vapour concentrations are considerably lower, since an important source of water vapour (CH_4 oxidation) is not considered in the model. These differences affect the temperature distribution, the wind field and the polar vortices. However, the overall differences in the stratospheric climate are small.

3.2 Tropospheric and surface changes

In the troposphere, significant temperature differences are only found during the austral spring season in the southern high latitudes below 250 hPa (Fig. 4). The warming is related to differences in the cloud cover between CHEM and NOCHEM. During austral winter and spring significantly more clouds are formed in CHEM, with differences up to 20 % in the vertical integrated total cloud cover. The additional clouds are mainly limited to areas southward of 60° S and altitudes between 250 and 100 hPa, covering the lower stratosphere and upper troposphere. These clouds are a consequence of the higher stratospheric water vapour concentration due to the oxidation of CH_4 in the chemistry module. Under the cold conditions of the polar night, the available water vapour condenses to ice clouds, which absorb and reflect a fraction of the outgoing longwave radiation and warm the air column below. The clouds are formed during the winter season and reach their largest coverage in August. Similarly, the radiation balance changes in time and the temperature anomaly peaks in August. The tropospheric temperature anomaly is therefore still weak and not significant during austral winter, but has a clear and significant impact on the temperatures in austral spring.

GMDD
7, 3013–3084, 2014

A similar effect is found in the NH for the boreal winter. However, here the effect is smaller, since the cooling in the polar stratosphere is smaller over the Arctic than over Antarctica and less clouds are formed.

Differences in the tropospheric zonal mean wind reveal a more heterogeneous pattern. In the SH, the reduced meridional temperature gradient in spring causes a shift of the westerlies to the equator, with a significant reduction in the south and (insignificant) increases in the north. However, during austral summer and autumn the westerly circulation is stronger in the south (sign. in MAM). In the NH, a significant weakening of the westerlies at high latitudes is also found for MAM together with a strengthening in summer.

At the surface the differences between CHEM and NOCHEM are smaller and only a few significant changes are found (Fig. 5). In the Barents Sea, higher temperatures in CHEM are present during the entire year and related to less sea ice (Fig. 5). The variability in the sea ice cover in the Barents Sea is in general very large. The sea level pressure or wind patterns reveal no consistent changes that may help to explain the differences. Differences between CHEM and NOCHEM in this region are therefore probably related to internal processes in the ocean that modulate the inflow of warm Atlantic water into the Barents Sea basin and, consequently, the sea ice cover and the surface temperatures.

In the SH high latitudes, the higher temperatures in CHEM during austral spring is obviously related to the cloud cover differences as explained above. In the Southern Ocean, between Australia and Antarctica a cooling is present during the entire year.

In the North Atlantic sea level pressure (SLP) significantly increases in CHEM compared to NOCHEM (Fig. 5). In the North Pacific a significant reduction of the SLP is found for MAM and a significant increase for the SON season. No significant changes are found for the SLP field in the SH, except for austral spring, which is related to the temperature differences between CHEM and NOCHEM.

Besides changes in the mean climate, the missing interannual variability in the ozone concentration may also influence the variability at the surface. However, the surface

GMDD
7, 3013–3084, 2014

temperatures do not show a systematic and significant change in the variability for any season (not shown).

The variance ratio between CHEM and NOCHEM of the SLP field is shown in Fig. 6. In the NH, the centres of action that modulate weather and climate during the winter months are the North Atlantic (Iceland low and Azores high) and the Aleutian low. No significant influence of the interactive chemistry in these highly variable regions is found. During the other seasons, some significant changes are detected, but mainly in regions with an overall low variability (e.g., in the tropics). The reasons for these changes are unclear. In the SH mid- and high latitudes the variability is increased in all seasons except autumn, however, the regions with significant increases change from season to season.

For the ocean no significant differences between CHEM and NOCHEM are found, besides the above mentioned sea ice cover anomalies in the Barents Sea (not shown). The ocean is therefore not affected by the interactive atmospheric chemistry.

In summary, the influence of the interactive chemistry in the troposphere is regionally and seasonally limited. The largest difference between CHEM and NOCHEM, the change in winter and spring climate over Antarctica, is related to the differences in stratospheric water vapour concentrations between the two experiments. Significant and consistent influences of the chemistry on the variability are rare.

3.3 Climate sensitivity of SOCOL-MPIOM

The climate sensitivity is the temperature response after a perturbation in the radiative forcing. Knowledge about the climate sensitivity of a model is crucial for the interpretation of transient climate simulations past and future climates. Several methods can be applied to estimate the climate sensitivity of a model. We focus here on two approaches, the transient climate response (TCR) and the equilibrium climate sensitivity (ECS).

In Fig. 7 both measures are compared to the TCR and ECS values of the CMIP5 ensemble. With 2.2 K the TCR of SOCOL-MPIOM is in the range of the higher sensitivities

GMDD
7, 3013–3084, 2014

of the CMIP5 ensemble. For the configuration without interactive chemistry, which is forced by a perpetual 1990 ozone climatology a second double CO_2 simulation lead to the slightly larger TCR of 2.3 K. Hence, the interactive chemistry module has only minor influences on the TCR of SOCOL-MPIOM. The ECS has been estimated from the CO_2 quadrupling experiments (Andrews et al., 2012). With 4.2 K it is also among the models with the high climate sensitivity. Still, the estimate is within the sensitivity range from 1.5 to 4.5 K (Stocker et al., 2013).

In comparison to the MPI-ESM based on ECHAM5–MPIOM, the TCR is the same but the ECS is considerably higher. For the IPCC AR4 Randall et al. (2007) reported a TCR of 2.2 K and an ECS of 3.4 K, for a configuration with higher spatial resolution (T63L39 in the atmosphere and approx. $1.5^\circ \times 1.5^\circ$ in the ocean). For a configuration with the same spatial resolution in the atmosphere and the ocean, but a lower vertical resolution in the atmosphere, Li et al. (2012) reported an ECS of 3.7 K. They also showed that the approach by Gregory et al. (2004) might lead to an overestimation of the ECS in the order of 10 % and proposed an improved methodology that takes the tendency of the deep-ocean heat uptake (ocean below 1500 m) into account. At the end of the 150 year experiment, the heat uptake is clearly positive and the correction proposed by Li et al. (2012) results in a lower value of 3.7 K, which corresponds better with the estimate of Li et al. (2012). Still, the value is in the upper range of the CMIP5 ensemble.

4 Transient climate simulations

In this section we present results from an ensemble of transient climate simulations performed with the AOCCM SOCOL-MPIOM for the periods 1600–2000. Three periods will be analysed in detail focusing on the surface air temperature (SAT): the early pre-industrial period with the two pronounced solar minima, namely the late Maunder Minimum (MM, 1670–1699) and the Dalton Minimum (DM, 1800–1829), and the

GMDD
7, 3013–3084, 2014

industrial period (1850–2000), which is highly influenced by anthropogenic emissions of GHGs.

4.1 Temperature variability in the pre-industrial period

The NH mean temperature in the four transient simulations is compared to proxy reconstructions in Fig. 8. The shading represent the probability range of the NH temperature variations based on multiple proxies (Jansen et al., 2007). Values are expressed as as anomalies from the mean over the pre-industrial period 1600–1850. First the temperature variability in the pre-industrial period is assessed.

The simulations show both agreement and disagreement for certain periods. For the entire pre-industrial period, the simulations exhibit pronounced multi-decadal scale temperature variations. On a decadal scales, the influence of volcanic eruptions on these variations is large. In the 17 century, the first signal common in all simulations is a temperature increase from the year 1600 onwards, which is related to the recovery after the volcanic eruption in the first simulation year (1600, Huaynaputina). Also the eruption in the year 1641 (Parker) is clearly visible in the simulations and the reconstructions. From 1650 onwards the negative trend in the solar forcing, leading into the MM, becomes visible. The lowest MM values are reached approximately around the year 1700, but the variability between the simulations is large. Although the large solar forcing differences (up to 3 Wm^{-2}) are not visible for the lowest values of the MM, the effect of the solar forcing becomes apparent when the temperatures between the beginning and the end of the 17 century is compared (Table 4). For the first three vs. the last three decades of the 17 century, the NH mean temperature is reduced by −0.34 K and −0.40 K in L1 and L2, respectively, and by −0.24 K and −0.03 K for M1 and M2, respectively. Contrary to the simulations, the MM is barely visible in the reconstruction as the so called Little Ice Age starts before the 17 century. Using a different approach, but a similar set of temperature proxies for the NH, Frank et al. (2010) identified the period 1601–1630 as the coldest 30 years of the last millennium. Consequently, no

GMDD
7, 3013–3084, 2014

additional cooling can be found towards the end of the 17 century and the temperature differences between 1600–1629 and 1670–1699 is +0.03 K.

It should be mentioned that the temperature variations in the MM may also be influenced by the artificially stable 1600 AD conditions from the control run, which are used to initialize the transient simulations. This may result in an unrealistic climate state at the beginning of the 17 century that complicates the comparison with the reconstructions.

With the end of the MM the NH mean temperatures start to increase again, following the increasing trend in the radiative forcing from the sun. This increase is again larger compared to the reconstructions and suspended for multiple years by several volcanic eruptions. The most prominent example is the temperature reductions after the Katla eruption on Iceland (1755) and the eruption of Makian in Indonesia (1761), which cause a pronounced NH cooling for several years, although their total aerosol mass is relatively small (Gao et al., 2008). For the post MM temperature increase, the differences between the two solar forcings are not very pronounced (Table 4) and for both solar forcings the temperature amplitudes are overestimated by a factor of 2 or larger, in comparison to the reconstructions.

From 1800 onwards, the solar energy input decreases again with the onset of the DM. This period is clearly dominated by the two volcanic eruptions 1809 (unknown) and 1815 (Tambora) as well as the eruption pair 1831 and 1835 (Babuyan Claro and Cosiguina). For the DM the differences in the two solar forcing reconstructions (up to 2.5 $W m^{-2}$) are not reflected in the NH averaged temperatures and the agreement with the reconstructions is better.

The internal variability is an important factor that complicates the identification of the fingerprints of external forcings in the climate system. For climate models, the technique of ensemble simulations allows to extract the forcing signal. To reliably exclude any signal of internal variability, the number of simulations has to be sufficiently large. An ensemble size of 2 is clearly too small to get robust estimates of the signals caused by external forcings. Still, we average over each ensemble in the following to increase

GMDD
7, 3013–3084, 2014

the signal-to-noise ratio. Using the two ensembles, L and M, we compare the spatial patterns for the MM and the DM against the patterns found in reconstructions. As reference period, which should represent an undisturbed pre-industrial situation relative to the two solar minima, the period 1770–1799 is selected. During these 30 years the solar irradiance values are very similar in both forcing datasets and also comparable to present day values (Fig. 1). Furthermore, no large volcanic eruption took place. For the solar minima, we select a 30 yr window roughly around the lowest TSI values, i.e. the period 1670–1699 for the late MM and the period 1800–1829 for the DM. Anomalies for these periods are compared to the spatial multi-proxy based temperature reconstructions of Mann et al. (2009).

The reconstructed temperatures during the MM are stronger reduced in the NH than in the SH, with the lowest temperatures over the North American continent and over northern Europe (Fig. 9e). Weak positive anomalies are also found, but they are not significant. Similar to the hemispheric mean time series, the cooling signal during the MM is more pronounced in both ensembles (Fig. 9a and b). The simulated MM temperature anomalies are almost everywhere negative and significant. For the L-forcing, the anomalies are slightly more pronounced than for the M-forcing, but the difference is small, which agrees with the findings for the hemispheric means (Table 4).

For the DM, the reconstructed temperature pattern is similar to the MM, with a larger cooling in the NH and the largest anomalies in North America and Scandinavia (Fig. 9f). Overall the cooling is weaker than during the MM. The simulated patterns are less homogeneous and the differences between the two ensembles are larger (Fig. 9c and d). Nevertheless, both ensembles resemble the cold anomalies of the reconstruction. Large areas of cold anomalies are found in the tropics and over the Barents Sea, where sea ice increases (not shown). Despite the cold anomalies, significant warmer conditions are found in the Labrador Sea (M-forcing) or the North Atlantic (L-forcing), which are not present in the reconstructions and may be related to internal variability of the ocean circulation or a response of the Atlantic meridional overturning to the volcanic forcing (e.g. Mignot et al., 2011). Overall the agreement to the reconstructions is

GMDD
7, 3013–3084, 2014

better for the DM than for the MM, although for both periods the simulated temperature anomalies are more pronounced.

Note that for the NH hemispheric average (Fig. 8) the centennial variations in Mann et al. (2009) are not very pronounced and represent mainly the median of Jansen et al. (2007).

Whereas the agreement during the DM is rather good, the MM temperature reductions are in the lowest probability range of the reconstructions. During the DM, temperature reductions are dominated by several volcanic eruptions, but the solar forcing reduction is less strong and shorter compared to the MM. Therefore, the influence of the solar variability is probably more pronounced during the MM and better separated from volcanic signals, than in the DM. For L1 and L2 the solar signal is obvious in both members during the MM. For M1 and M2 one member simulates nearly no cooling during the MM, despite a forcing reduction of up to $3\,W\,m^{-2}$ for several decades. This indicates that the internal variability of the climate system might compensate even large variations in the external forcing.

The relative contributions of the solar and the volcanic forcing for the temperature variations during the DM is difficult to extract from the transient experiments. However, using SOCOL-MPIOM Anet et al. (2013a, b) showed that the temperature reduction in the DM is mainly related to the variability in the visible part of the solar spectrum and volcanic eruptions. The UV variability is not important for the surface climate. The volcanic forcing cools the climate mainly in the tropics and is larger in the SH than in the NH, which is related to the asymmetric distribution of the aerosol cloud of the Tambora eruption.

4.2 Temperature trends after 1850

A significant anthropogenic influence on the global mean temperature starts at the latest with the beginning of the industrialization, i.e., approximately since the mid of the 19 century. Moreover, a sufficient number of instrumental based weather observations are available since the mid 19 century so that it is possible to derive global mean surface

GMDD
7, 3013–3084, 2014

temperatures (Brohan et al., 2006; Hansen et al., 2010) or to apply them in data assimilation projects (Compo et al., 2011). For a climate model, the ability to reproduce these observed temperature trends is crucial. Therefore, the simulated temperature development since 1850 in the four transient simulations with SOCOL-MPIOM is described in the following.

4.2.1 Transient simulations

In the following the simulated surface air temperatures are compared to the observational data sets GISTEM and HadCRUT4 and to the 20 century reanalysis (20CR).

The global mean surface air temperature (SAT) increase is very similar in the two instrumental records and in the reanalysis (Fig. 10a). Before 1900 no positive trend is visible in the global mean SAT. In all records, the temperature increase of the 20 century is not continuous, but rather divided in two periods. The first increase is found between 1910 until 1940. This period is known as the early 20 century warming (Brönnimann, 2009). In 20CR this increase starts at the same time, but is slightly weaker. After 1940 the global mean temperature rise is reduced or even suspended for about two decades. Finally, from 1960 onwards a clearly positive temperature trend is found in all data sets. In the instrumental records the temperature increase in the first half of the 20 century and the cold period around 1950 are more pronounced than in 20CR.

The simulated mean SAT increase since 1850 is much stronger in all transient simulations than in the observations. From around 1900 onwards temperatures increase more or less linear, with a slight acceleration after 1960. The surface temperature trends are very similar in all four experiments. In particular, no substantial difference between model results obtained with medium and large amplitude solar forcing is found, although the difference in the increase in the TSI values during the 20 century is up to 1.7 $\mathrm{W\,m^{-2}}$ (TOA). However, in the ocean heat uptake, the difference between the two forcings is clearly visible. Furthermore, stronger increases in the outgoing longwave radiation in the L simulations partly compensate the forcing difference. To reduce

GMDD
7, 3013–3084, 2014

complexity, we concentrate on the medium solar forcing amplitude simulations in the following.

The pattern of the temperature changes might help to identify differences to the observed records. Furthermore, regions with pronounced temperature increase that may be associated with positive feedbacks can be identified. Therefore, we compare the temperature difference between a 30 yr period at the beginning (1890–1919) and at the end of the 20 century (1970–1999). The results are however not sensitive to the exact choice of the periods and a trend pattern analysis also leads to similar results.

A comparison of the pattern of the SAT increase in the 20 century is given in Fig. 11. In the observations significant positive temperature changes can be found over the entire globe, interrupted by regions without any changes or significant temperature reductions. Over the oceans a warming is obvious almost everywhere. The largest temperature increases are found in the Southern Ocean at mid latitudes, reaching around $2\,K\,100\,yr^{-1}$. In general differences between the records are small over the ocean. This is to some degree expected, since, e.g., 20CR used the same SST records (HadSST) as HadCRUT4 as lower boundary condition. Over the continent, the pattern is spatially more heterogeneous, but regions with significant positive temperature increases are found on all continents. In 20CR regions with temperature reductions are more pronounced than in the other two records.

In comparison to HadCRUT4 and GISTEMP the changes in the southern and in particular in the northern polar region are much stronger in 20CR. For 20CR it is known that the Arctic temperature field suffers from a large, time-varying bias (Brönnimann et al., 2012) and an incorrect sea-ice distribution (Compo et al., 2011). However, also HadCRUT4 and GISTEMP are affected by a very low spatial and temporal coverage of instrumental based observations in these regions. These caveats should be considered when comparing trend estimates for the NH and SH polar regions.

In the simulations the strong signal in the global mean temperature is also apparent in the spatial pattern. The warming is too strong in many regions, and spatially very uniform. In the northern polar region, some signals of polar amplification can be found.

GMDD
7, 3013–3084, 2014

However, the differences in the global average are related to a strong and uniform warming over the entire globe and not to an overestimated polar amplification.

The spatially uniform warming may be related to a specific forcing like GHG or solar. The TCR of 2.2 K suggests a stronger temperature increase due to the anthropogenic GHG emissions in the 20 century. Contrary, results from Anet et al. (2013c) showed that the model response to the future GHG increase (RCP 4.5) is comparable to other CMIP5 models. In their experiments the temperature increase at the end of the 21 century (1.96 ± 0.12 K) is well in the range of the CMIP5 ensemble (1.8 ± 0.5 K, e.g., Knutti and Sedláček (2012)). Therefore, other forcings may contribute to the trend in the 20 century and amplify it.

4.2.2 Sensitivity to separated external forcings

The role of different forcings for the temperature trends since 1850 is evaluated using a number of sensitivity simulations where one external forcing or a combination of forcings is applied and the remaining forcings are held constant at pre-industrial levels (Table 1).

In doing so, the major GHGs, the solar activity, stratospheric and tropospheric aerosols and simulated ozone changes are investigated. In the troposphere, ozone concentration in general increased (Stevenson et al., 2013), whereas they are reduced by the emission of ozone depleting halogens in the stratosphere (Staehelin et al., 2001). Both changes have different effects on the radiation balance.

The contributions of the different forcings to the temperature trends is assessed by comparing the differences in the global mean temperatures between the two 30 yr periods defined above (1890–1919 and 1970–1999). The results are again not very sensitive to the exact choice of these periods.

In the full forcing experiment the mean temperature increase agrees well with the increases found in the two transient simulations (Fig. 10b). This gives us confidence, that the setup of the sensitivity experiments is able to reproduce the temperature behaviour, when all major forcings are considered. The major part of the temperature

GMDD
7, 3013–3084, 2014

increase simulated by all forcings is explained by the GHG forcing (73 %). The solar forcing (13 %) and the ozone trends (16 %) also contribute to the warming. The only negative signal (−15 %) is related to stratospheric and tropospheric aerosols. All individual forcings (solar, ozone, GHG, aerosols) add up to only 87 % of the full forcing experiment, suggesting that additional positive feedbacks are involved in the case of the full forcing experiment (e.g., sea ice albedo feedback).

To analyse the spatial structure of the global mean temperature differences, we compare again the difference pattern between the two 30 yr periods (Fig. 11). The warming is globally very uniform with some hints for polar amplifications in the northern high latitudes. This full forcing pattern is very similar to the changes of the GHG experiment, except for an overall larger trend. As in the global analysis, the GHG forcing dominates the full-forcing trend almost everywhere. The other three forcings display a much larger spatial heterogeneity and temperature changes are comparably small. The solar forcing, which, on global average, leads to a warming of approximately 0.13 K, has slightly significant contributions, e.g., over northern America, Greenland and Europa. Over Europe and North America the contributions from the solar forcing are clearly visible in the full forcing experiment. Further significant temperature increases are found in the tropical Atlantic and Indian Ocean. The aerosol forcing, which combines the influence of tropospheric and stratospheric aerosols, leads to significant negative temperature changes in the tropical continental areas of the SH and over a large region covering Russia and East Asia. Furthermore, a significant positive influence is found for the North Atlantic. Finally, the simulation forced by transient ozone changes reveals a significant and pronounced positive temperature increase in the NH high latitudes, which peaks over the Barents Sea. In the SH high latitudes, no comparable signal is found. Overall, several regions of significant positive temperature increases are associated with the ozone forcing.

The solar forcing used in the experiments accounts for an increase in the net radiative forcing (RF) of 0.28 $W m^{-2}$ (global average assuming a global mean albedo of 0.7), between the periods defined above. In the historical CMIP5 simulations the

GMDD
7, 3013–3084, 2014

corresponding forcing difference is only 0.09 $W m^{-2}$ (Lean, 2000; Wang et al., 2005). For the same periods, the RF from tropospheric ozone changes is estimated to be $0.4 \pm 0.2\,W m^{-2}$ (Myhre et al., 2013). The positive RF from tropospheric ozone is further compensated to some extent by the negative forcing from stratospheric ozone depletion, estimated to be around $-0.05 \pm 0.1\,W m^{-2}$ (Myhre et al., 2013). The combined RF from CO_2, CH_4, and N_2O (Ramaswamy et al., 2001), is 1.20 $W m^{-2}$ between 1989–1919 and 1970–1999.

Based on the RF and the temperature response ΔT we estimate a transient sensitivity parameter α [$K W^{-1} m^{-2}$], with $\alpha = \Delta T / RF$, for the three forcings. Values of α are estimated as 0.46 ± 0.25, 0.46 ± 0.25 and $0.58 \pm 0.08\,K W^{-1} m^{-2}$ for the solar, ozone (net RF: $0.30\,W m^{-2}$), and GHG experiment, respectively. The confidence interval is based on the 95 % confidence interval for the temperature response ΔT only. Note that the estimate is associated with further uncertainties related to the RF, in particular for ozone, and that ΔT is extracted from a single simulation. The analysis, thus, shows that the temperature response associated with the different forcings is consistent and the resulting signal is a combination of the climate sensitivity of SOCOL-MPIOM, the large solar forcing and the inclusion of the additional RF from the ozone chemistry.

5 Discussion and conclusions

This paper presents the coupled atmosphere-chemistry-ocean model SOCOL-MPIOM. The model is described using results from a number of simulations without changes in the external forcings (control simulations) and with transient external forcings for the period 1600–2000 AD.

Without changing external forcings the influence of the interactive chemistry module on the mean climate state and its variability is small and mainly confined to the stratosphere and mesosphere. The largest differences in the temperatures in the middle atmosphere are associated with several processes. First, the parametrization of the absorption in the Lyman-alpha, Schumann–Runge, Hartley, and Higgins bands is

GMDD
7, 3013–3084, 2014

responsible for a warmer mesosphere and higher stratosphere in the simulation with interactive chemistry. This parametrization is disabled in the configuration without interactive chemistry, but will be implemented in future version. Second, interactions between the diurnal variation in the mesospheric ozone concentrations and the radiation scheme lead to a cooling, partly compensating the aforementioned warming. Furthermore, stratospheric water vapour concentrations are higher with interactive chemistry due to the additional water vapour produced by the oxidation of methane in the chemistry module. Future version of the model configuration should therefore implement a parametrization of this process, e.g., similar to the approach in ECHAM 6 (Schmidt et al., 2013).

In the transient simulations for the period 1600–2000 the spectral solar forcing reconstructions of Shapiro et al. (2011) is tested and the simulations are compared to temperature reconstructions. To consider the uncertainty in the solar forcing, two different solar forcing data sets with large amplitude (corresponding to the mean forcing provided by Shapiro et al., 2011) and a medium amplitude (upper uncertainty envelope) are used. Both amplitudes are substantially larger than previous state-of-the-art solar forcing reconstructions. For the MM, the temperature response is in general larger than the signal found in reconstructions, whereas the agreement between proxies and simulations for the DM is better. The larger differences between reconstructions and model results in the MM may be related either to the MM being still affected by the model spin-up period or to the large amplitude of the solar forcing, with considerably larger variations than all other recent solar forcing reconstructions. During the DM, the period of reduced solar activity is shorter than during the MM and the solar effect is weaker. Instead, the volcanic forcing is the dominant driver for the surface temperature change.

The temperature variations in the transient simulations are always subject to internal variability and the influence of the solar forcing is therefore not directly visible in the hemispheric averages or the global mean for every solar minima. Likewise, the differences between the medium and the large amplitude solar forcing are not always

GMDD
7, 3013–3084, 2014

obvious. However, when the difference in the NH temperature between the simulations with medium and large solar forcing is calculated for all solar minima and maxima, the influence of the solar forcing becomes visible. Between 1600 and 2000, the sun went through three grand solar minima (MM, DM With a transient climate response (TCR) of 2.2 K and an equilibrium climate sensitivity (ECS) of 3.7 Kand Gleisberg minima) and four periods of higher solar activity. The temperature change for each of these periods, i.e., the temperature change from a solar minima to the following maxima or a maxima to the following minima, is significantly influenced by the TSI, except for the temperature reduction into the DM and the increase after the Gleisberg minimum. In these two cases strong other forcings, large volcanic eruption in the DM and the GHG increase after the Gleisberg minimum, dominate over the solar forcing. Averaged and normalized over all periods the simulated NH temperature change resulting from a change in the TSI is 0.06 $K W^{-1} m^{-2}$. When the two periods mentioned above are excluded, the response increases to 0.11 $K W^{-1} m^{-2}$.

With a transient climate response (TCR) of 2.2 K and an equilibrium climate sensitivity (ECS) of 3.7 K the sensitivity of SOCOL-MPIOM is on the higher side of the CMIP5 ensemble, but comparable to the related ECHAM5–MPIOM. The high sensitivity may also be influenced by the warm climate state used for the CO_2 perturbation experiments. The experiments are initialized using restart files for the year 1990 from the transient simulations. These transient runs are affected by a persistent positive temperature drift from the control simulation and an overestimation of the 20 century temperature increase. The climate state at the beginning of the CS experiments is therefore clearly too warm. Although the ECS is commonly assumed to be independent of the climate state, Meraner et al. (2013) showed that the climate state indeed has an influence on the ECS. In warmer climates, the ECS increases due to a stronger water vapour feedback.

The influence of the interactive chemistry on the TCR is very small but negative (~ -0.1 K). This is in agreement with results from Dietmüller et al. (2014). With the ECHAM/MESSy Atmospheric Chemistry (EMAC) model they found a reduction of the

GMDD
7, 3013–3084, 2014

climate sensitivity parameter by 3.4 % with interactive chemistry in the case of a (instantaneous) double CO_2 scenario. The reduction is explained by negative feedbacks introduced by the ozone chemistry with influences on the stratospheric water vapour. However, contrary to Dietmüller et al. (2014) who explained the feedback by reduction of the ozone concentrations in the lower tropical stratosphere of up to 20 %, the reductions in our experiments is much smaller (< 1 %).

In the industrial period, the climate sensitivity of the model in combination with the solar and the forcing from the ozone changes results in an overestimation of the temperature trends up to a factor of 2. Contrary to the solar forcing proposed for CMIP5 (Lean, 2000; Wang et al., 2005) and many other TSI reconstructions, the forcing of Shapiro et al. (2011) used in the transient simulations shows a strong increase in the radiative forcing from the sun in the first half of the 20 century. This increase is not within the confidence interval for the TSI changes presented in the last IPCC report (Myhre et al., 2013).

An additional positive signal comes from the simulated increase in the tropospheric ozone concentrations that also contribute to the global mean temperature trend. Estimates for the changes in global tropospheric ozone since pre-industrial times are rare and largely based on model simulations (Myhre et al., 2013). In comparison to other models the simulated tropospheric global ozone increase is stronger in this study. While SOCOL-MPIOM simulates increases in the order of 15 DU between the beginning and the end of the 20 century, Shindell et al. (2006) estimated an increase of around 10 DU. In a multi-model study with 17 different chemistry-climate models, Stevenson et al. (2013) found an increase of 8.4 DU between the 1850 and 2000th. Consequently, the effect on the temperature trends is larger, being 0.16 K in this study and ∼ 0.10 K in the simulation with the GISS model II (Shindell et al., 2006). However, the chemistry in the GISS model II is limited to levels below 150 hPa and parts of the tropical upper troposphere are not included. This may result in an underestimation of the effect by 20 %, as discussed by the authors (Shindell et al., 2006).

GMDD
7, 3013–3084, 2014

When only the radiative forcing from GHGs and the negative contributions from the aerosols are considered, the simulated warming would agree reasonably well with the observations. With the additional forcings used here, either the climate sensitivity of SOCOL-MPIOM would need to be lower or possible missing negative forcings would need to be included to match the observed temperature trends.

Despite the lack of a full understanding of the strong transient climate response and equilibrium climate sensitivity of the new model, with the coupling of SOCOL-MPIOM a novel atmosphere-chemistry-ocean model has been developed that allows the inclusion of chemistry-climate feedbacks in long-term simulations for the past and the future. Furthermore, with a configuration that allows the deactivation of the chemistry scheme the influence of the chemistry–climate feedbacks in the climate can be assessed. Earlier studies with SOCOL-MPIOM highlighted the relevance of the atmospheric chemistry in climate model simulations (Anet et al., 2013a, b, c; Muthers et al., 2014). Under conditions without a change in the external forcings, the influence of the interactive chemistry on the climate state is small. Future work will concentrate on the role of chemistry–climate feedbacks under changing external forcings.

Acknowledgements. The authors thank the Max–Planck Institute for Meteorology in Hamburg, Germany, in particular Johann Jungclaus and Helmuth Haak, for providing the restart files from the Millennium Simulations and the technical support. This work has been supported by the Swiss National Science Foundation under grant CRSI122-130642 (FUPSOL), CRSII2-147659 (FUPSOL II) and under grant CRSI22-130642 21 (FuMES), as well as by the CCES project MAIOLICA-2. E. Rozanov and W. Schmutz would like to acknowledge the support of the project by State Secretariat for Education, Research and Innovation (SERI) of Swiss Confederation under the grant C11.01124 (project SOVAC). ECMWF ERA-40 data used in this study have been obtained from the ECMWF Data Server. This paper profited from discussions during the PAGES/FUPSOL Workshop in 2012.

GMDD
7, 3013–3084, 2014

References

Andrews, T., Gregory, J. M., Webb, M. J., and Taylor, K. E.: Forcing, feedbacks and climate sensitivity in CMIP5 coupled atmosphere–ocean climate models, Geophys. Res. Lett., 39, L09712, doi:10.1029/2012GL051607, 2012. 3040

Anet, J. G., Muthers, S., Rozanov, E., Raible, C. C., Peter, T., Stenke, A., Shapiro, A. I., Beer, J., Steinhilber, F., Brönnimann, S., Arfeuille, F., Brugnara, Y., and Schmutz, W.: Forcing of stratospheric chemistry and dynamics during the Dalton Minimum, Atmos. Chem. Phys., 13, 10951–10967, doi:10.5194/acp-13-10951-2013, 2013a. 3018, 3044, 3053

Anet, J. G., Muthers, S., Rozanov, E. V., Raible, C. C., Stenke, A., Shapiro, A. I., Brönnimann, S., Arfeuille, F., Brugnara, Y., Beer, J., Steinhilber, F., Schmutz, W., and Peter, T.: Impact of solar vs. volcanic activity variations on tropospheric temperatures and precipitation during the Dalton Minimum, Clim. Past Discuss., 9, 6179–6220, doi:10.5194/cpd-9-6179-2013, 2013b. 3016, 3044, 3053

Anet, J. G., Rozanov, E. V., Muthers, S., Peter, T., Brönnimann, S., Arfeuille, F., Beer, J., Shapiro, A. I., Raible, C. C., Steinhilber, F., and Schmutz, W. K.: Impact of a potential 21 century "grand solar minimum" on surface temperatures and stratospheric ozone, Geophys. Res. Lett., 40, 4420–4425, doi:10.1002/grl.50806, 2013c. 3047, 3053

Arfeuille, F., Weisenstein, D., Mack, H., Rozanov, E., Peter, T., and Brönnimann, S.: Volcanic forcing for climate modeling: a new microphysics-based data set covering years 1600–present, Clim. Past, 10, 359–375, doi:10.5194/cp-10-359-2014, 2014. 3026, 3073

Baldwin, M. P. and Dunkerton, T. J.: Propagation of the Arctic Oscillation from the stratosphere to the troposphere, J. Geophys. Res., 104, 30937–30946, doi:10.1029/1999JD900445, 1999. 3015

Baldwin, M. P. and Dunkerton, T. J.: Stratospheric harbingers of anomalous weather regimes, Science, 294, 581–4, doi:10.1126/science.1063315, 2001. 3016

Baldwin, M. P., Cheng, X., and Dunkerton, T. J.: Observed correlations between winter-mean tropospheric and stratospheric circulation anomalies, Geophys. Res. Lett., 21, 1141–1144, 1994. 3016

Baldwin, M. P., Dameris, M., and Shepherd, T. G.: How will the stratosphere affect climate change?, Science, 316, 1576–1577, 2007. 3015

Baumgaertner, A. J. G., Jöckel, P., and Brühl, C.: Energetic particle precipitation in ECHAM5/MESSy1 – Part 1: Downward transport of upper atmospheric NO_x produced by

GMDD
7, 3013–3084, 2014

low energy electrons, Atmos. Chem. Phys., 9, 2729–2740, doi:10.5194/acp-9-2729-2009, 2009. 3027
Breiteig, T.: Extra-tropical synoptic cyclones and downward propagating anomalies in the Northern Annular Mode, Geophys. Res. Lett., 35, L07809, doi:10.1029/2007GL032972, 2008. 3035
Brohan, P., Kennedy, J. J., Harris, I., Tett, S. F. B., and Jones, P. D.: Uncertainty estimates in regional and global observed temperature changes: a new data set from 1850, J. Geophys. Res., 111, D12106, doi:10.1029/2005JD006548, 2006. 3029, 3030, 3045
Brönnimann, S.: Early twentieth-century warming, Nat. Geosci., 2, 735–736, doi:10.1038/ngeo670, 2009. 3045
Brönnimann, S., Annis, J. L., Vogler, C., and Jones, P. D.: Reconstructing the quasi-biennial oscillation back to the early 1900s, Geophys. Res. Lett., 34, L22805, doi:10.1029/2007GL031354, 2007. 3023, 3027
Brönnimann, S., Grant, A. N., Compo, G. P., Ewen, T., Griesser, T., Fischer, A. M., Schraner, M., and Stickler, A.: A multi-data set comparison of the vertical structure of temperature variability and change over the Arctic during the past 100 years, Clim. Dynam., 39, 1577–1598, doi:10.1007/s00382-012-1291-6, 2012. 3046
Budich, R., Gioretta, M., Jungclaus, J., Redler, R., and Reick, C.: The MPI-M Millennium Earth System Model: An assembling Guide for the COSMOS Configuration, MPI report, Max-Planck Institute for Meteorology, Hamburg, Germany, 2010. 3022
Cagnazzo, C., Manzini, E., Giorgetta, M. A., Forster, P. M. De F., and Morcrette, J. J.: Impact of an improved shortwave radiation scheme in the MAECHAM5 General Circulation Model, Atmos. Chem. Phys., 7, 2503–2515, doi:10.5194/acp-7-2503-2007, 2007. 3019
Calisto, M., Usoskin, I., Rozanov, E., and Peter, T.: Influence of Galactic Cosmic Rays on atmospheric composition and dynamics, Atmos. Chem. Phys., 11, 4547–4556, doi:10.5194/acp-11-4547-2011, 2011. 3021
Charlton, A. J. and Polvani, L. M.: A new look at stratospheric sudden warmings, Part I: Climatology and modeling benchmarks, J. Climate, 20, 449–470, 2007. 3035, 3071
Compo, G. P., Whitaker, J. S., Sardeshmukh, P. D., Matsui, N., Allan, R. J., Yin, X., Gleason, B. E., Vose, R. S., Rutledge, G., Bessemoulin, P., Brönnimann, S., Brunet, M., Crouthamel, R. I., Grant, a. N., Groisman, P. Y., Jones, P. D., Kruk, M. C., Kruger, a. C., Marshall, G. J., Maugeri, M., Mok, H. Y., Nordli, O., Ross, T. F., Trigo, R. M., Wang, X. L.,

GMDD
7, 3013–3084, 2014

Woodruff, S. D., and Worley, S. J.: The Twentieth Century Reanalysis project, Q. J. Roy. Meteor. Soc., 137, 1–28, doi:10.1002/qj.776, 2011. 3029, 3045, 3046
Cordero, E. C. and Forster, P. M. de F.: Stratospheric variability and trends in models used for the IPCC AR4, Atmos. Chem. Phys., 6, 5369–5380, doi:10.5194/acp-6-5369-2006, 2006. 3015
Cubasch, U., Meehl, G., Boer, G., Stouffer, R., Dix, M., Noda, A., Senior, C., Raper, S., Yap, K., Abe-Ouchi, A., Brinkop, S., Claussen, M., Collins, M., Evans, J., Fischer-Bruns, I., Flato, G., Fyfe, J., Ganopolski, A., Gregory, J., Hu, Z.-Z., Joos, F., Knutson, T., Knutti, R., Landsea, C., Mearns, L., Milly, C., Mitchell, J., Nozawa, T., Paeth, H., Räisänen, J., Sausen, R., Smith, S., Stocker, T., Timmermann, A., Ulbrich, U., Weaver, A., Wegner, J., Whetton, P., Wigley, T., Winton, M., and Zwiers, F.: Projections of future climate change, in: Climate Change 2001: The Scientific Basis, 525–582, Cambridge University Press, 2001. 3024
Dee, D. P., Uppala, S. M., Simmons, A. J., Berrisford, P., Poli, P., Kobayashi, S., Andrae, U., Balmaseda, M. A., Balsamo, G., Bauer, P., Bechtold, P., Beljaars, A. C. M., van de Berg, L., Bidlot, J., Bormann, N., Delsol, C., Dragani, R., Fuentes, M., Geer, A. J., Haimberger, L., Healy, S. B., Hersbach, H., Hólm, E. V., Isaksen, L., Kållberg, P., Köhler, M., Matricardi, M., McNally, A. P., Monge-Sanz, B. M., Morcrette, J.-J., Park, B.-K., Peubey, C., de Rosnay, P., Tavolato, C., Thépaut, J.-N., and Vitart, F.: The ERA-Interim reanalysis: configuration and performance of the data assimilation system, Q. J. Roy. Meteor. Soc., 137, 553–597, doi:10.1002/qj.828, 2011. 3029, 3070
Dietmüller, S., Ponater, M., and Sausen, R.: Interactive ozone induces a negative feedback in CO_2 driven climate change simulations, J. Geophys. Res., 119, 1796–1805, doi:10.1002/2013JD020575, 2014. 3051, 3052
Driscoll, S., Bozzo, A., Gray, L. J., Robock, A., and Stenchikov, G.: Coupled Model Intercomparison Project 5 (CMIP5) simulations of climate following volcanic eruptions, J. Geophys. Res., 117, D17105, doi:10.1029/2012JD017607, 2012. 3034, 3035, 3070
Egorova, T., Rozanov, E., Zubov, V., and Karol, I. L.: Model for investigating ozone trends (MEZON), Izvestiya, Atmos. Ocean. Phys., 39, 277–292, 2003. 3019
Egorova, T., Rozanov, E., Manzini, E., Schmutz, W., and Peter, T.: Chemical and dynamical response to the 11-year variability of the solar irradiance simulated with a chemistry-climate model, Geophys. Res. Lett., 83, 6225–6230, doi:10.1029/2003GL019294, 2004. 3020

GMDD
7, 3013–3084, 2014

Etheridge, D., Steele, L., Langenfelds, R., Francey, R., Barnola, J., and Morgan, V.: Natural and anthropogenic changes in atmospheric CO2 over the last 1000 years from air in Antarctic ice and firn, J. Geophys. Res., 101, 4115–4128, doi:10.1029/95JD03410, 1996. 3025

Etheridge, D. M., Steele, L. P., Francey, R. J., and Langenfelds, R. L.: Atmospheric methane between 1000 AD, and present: evidence of anthropogenic emissions and climatic variability, J. Geophys. Res., 103, 15979–15993, doi:10.1029/98JD00923, 1998. 3025

Eyring, V., Butchart, N., Waugh, D. W., Akiyoshi, H., Austin, J., Bekki, S., Bodeker, G. E., Boville, B. A., Brühl, C., Chipperfield, M. P., Cordero, E., Dameris, M., Deushi, M., Fioletov, V. E., Frith, S. M., Garcia, R. R., Gettelman, A., Giorgetta, M. A., Grewe, V., Jourdain, L., Kinnison, D. E., Mancini, E., Manzini, E., Marchand, M., Marsh, D. R., Nagashima, T., Newman, P. A., Nielsen, J. E., Pawson, S., Pitari, G., Plummer, D. A., Rozanov, E., Schraner, M., Shepherd, T. G., Shibata, K., Stolarski, R. S., Struthers, H., Tian, W., and Yoshiki, M.: Assessment of temperature, trace species, and ozone in chemistry-climate model simulations of the recent past, J. Geophys. Res., 111, D22308, doi:10.1029/2006JD007327, 2006. 3018

Ferretti, D. F., Miller, J. B., White, J. W. C., Etheridge, D. M., Lassey, K. R., Lowe, D. C., Meure, C. M. M. F., Dreier, M. F., Trudinger, C. M., Van Ommen, T. D., and Langenfelds, R. L.: Unexpected changes to the global methane budget over the past 2000 years, Science, 309, 1714–1717, doi:10.1126/science.1115193, 2005. 3025

Fischer, A. M., Schraner, M., Rozanov, E., Kenzelmann, P., Schnadt Poberaj, C., Brunner, D., Lustenberger, A., Luo, B. P., Bodeker, G. E., Egorova, T., Schmutz, W., Peter, T., and Brönnimann, S.: Interannual-to-decadal variability of the stratosphere during the 20th century: ensemble simulations with a chemistry-climate model, Atmos. Chem. Phys., 8, 7755–7777, doi:10.5194/acp-8-7755-2008, 2008. 3036

Flato, G., Marotzke, J., Abiodun, B., Braconnot, P., Chou, S., Collins, W., Cox, P., Driouech, F., Emori, S., Eyring, V., Forest, C., Gleckler, P., Guilyardi, E., Jakob, C., Kattsov, V., Reason, C., and Rummukainen, M.: Evaluation of climate models, in: Climate Change 2013: The Physical Science Basis, Contribution of Working Group I to the Fifth Assessment Report of the Intergovernmental Panel on Climate Change, edited by: Stocker, T., Qin, D., Plattner, G.-K., Tignor, M., Allen, S., Boschung, J., Nauels, A., Xia, Y., Bex, V., and Midgley, P., chap. 6, Cambridge University Press, Cambridge, UK and New York, NY, USA, 741–866, 2013. 3015, 3080

Fouquart, Y. and Bonnel, B.: Computations of solar heating of the Earth's atmosphere: a new parameterization, Beitr. Phys. Atmos., 53, 35–62, 1980. 3019

GMDD
7, 3013–3084, 2014

Frank, D. C., Esper, J., Raible, C. C., Büntgen, U., Trouet, V., Stocker, B., and Joos, F.: Ensemble reconstruction constraints on the global carbon cycle sensitivity to climate, Nature, 463, 527–30, doi:10.1038/nature08769, 2010. 3041

Gabriel, A., Peters, D., Kirchner, I., and Graf, H.-F.: Effect of zonally asymmetric ozone on stratospheric temperature and planetary wave propagation, Geophys. Res. Lett., 34, L06807, doi:10.1029/2006GL028998, 2007. 3021

Gao, C., Robock, A., and Ammann, C.: Volcanic forcing of climate over the past 1500 years: an improved ice core-based index for climate models, J. Geophys. Res., 113, D23111, doi:10.1029/2008JD010239, 2008. 3027, 3042

Gerber, E. P., Butler, A., Calvo, N., Charlton-Perez, A., Giorgetta, M., Manzini, E., Perlwitz, J., Polvani, L. M., Sassi, F., Scaife, A. A., Shaw, T. A., Son, S.-W., and Watanabe, S.: Assessing and understanding the impact of stratospheric dynamics and variability on the earth system, B. Am. Meteorol. Soc., 93, 845–859, doi:10.1175/bAms-d-11-00145.1, 2012. 3015, 3016

Gillett, N. P. and Thompson, D. W. J.: Simulation of recent Southern Hemisphere climate change, Science, 302, 273–5, doi:10.1126/science.1087440, 2003. 3015, 3017

Gillett, N. P., Allen, M. R., McDonald, R. E., Senior, C. A., Shindell, D. T., and Schmidt, G. A.: How linear is the Arctic Oscillation response to greenhouse gases?, J. Geophys. Res., 107, 1–7, doi:10.1029/2001JD000589, 2002. 3015

Giorgetta, M. A., Bengtsson, L., and Arpe, K.: An investigation of QBO signals in the east Asian and Indian monsoon in GCM experiments, Clim. Dynam., 15, 435–450, doi:10.1007/s003820050292, 1999. 3017, 3020

Graf, H.-F., Kirchner, I., Robock, A., and Schult, I.: Pinatubo eruption winter climate effects: Model vs. observations, Clim. Dynam., 92, 81–93, 1993. 3016

Graversen, R. G. and Christiansen, B.: Downward propagation from the stratosphere to the troposphere: a comparison of the two hemispheres, J. Geophys. Res., 108, 1–10, doi:10.1029/2003JD004077, 2003. 3015

Gray, L. J., Scaife, A. A., Mitchell, D. M., Osprey, S., Ineson, S., Hardiman, S. C., Butchart, N., Knight, J., Sutton, R., and Kodera, K.: A lagged response to the 11-year solar cycle in observed winter Atlantic/European weather patterns, J. Geophys. Res., 24, 13,405–13,420, doi:10.1002/2013JD020062, 2013. 3016

Gregory, J. M., Ingram, W. J., Palmer, M. A., Jones, G. S., Stott, P. A., Thorbe, R. B., Lowe, J. A., Johns, T. C., and Williams, K. D.: A new method for diagnosing radiative forcing and climate

GMDD
7, 3013–3084, 2014

sensitivity, Geophys. Res. Lett., 31, L03205, doi:10.1029/2003GL018747, 2004. 3024, 3040, 3080
Hagemann, S.: An improved land surface parameter dataset for global and regional climate models, MPI report 336, Max-Planck Institut fuer Meteorologie, Hamburg, Germany, 2002. 3023, 3027
Hagemann, S. and Duemenil, L.: A parameterisation of the lateral waterflow for the global scale, Clim. Dynam., 14, 17–31, 1998. 3020
Hagemann, S. and Duemenil-Gates, L.: Improving a subgrid runoff parameterisation scheme for climate models by the use of high resolution data derived from satellite observations, Clim. Dynam., 21, 349–359, 2003. 3020
Haigh, J. D.: The role of stratospheric ozone in modulating the solar radiative forcing of climate, Nature, 370, 544–546, doi:10.1038/370544a0, 1994. 3016, 3017, 3018
Haigh, J. D.: The impact of solar variability on climate, Science, 272, 981–984, 1996. 3016
Haigh, J. D., Blackburn, M., and Day, R.: The response of tropospheric circulation to perturbations in lower-stratospheric temperature, J. Climate, 18, 3672–3685, 2005. 3016
Hansen, J., Ruedy, R., Sato, M., Lo, K., Met Office, and Hadley Center: Global surface temperature change, Rev. Geophys., 48, 1–29, doi:10.1029/2010RG000345, 2010. 3029, 3045
Hardiman, S. C., Butchart, N., Hinton, T. J., Osprey, S. M., and Gray, L. J.: The effect of a well-resolved stratosphere on surface climate: differences between CMIP5 simulations with high and low top versions of the Met Office Climate Model, J. Climate, 25, 7083–7099, doi:10.1175/JCLI-D-11-00579.1, 2012. 3015
Hoyle, C. R.: Three dimensional chemical transport model study of ozone and related gases 1960–2000, Ph.D. thesis, Eidgenössische Technische Hochschule, Zürich, Switzerland, 2005. 3019
Hu, Y. and Tung, K. K.: Possible ozone-induced long-term changes in planetary wave activity in late winter, J. Climate, 16, 3027–3038, 2003. 3018
Hurrell, J. W.: Decadal trends in the North Atlantic Oscillation: regional temperatures and precipitation, Science, 269, 676–679, 1995. 3016
Jackman, C. H., Marsh, D. R., Vitt, F. M., Garcia, R. R., Randall, C. E., Fleming, E. L., and Frith, S. M.: Long-term middle atmospheric influence of very large solar proton events, J. Geophys. Res.-Atmos., 114, 304, doi:10.1029/2008JD011415, 2009. 3027
Jansen, E., Overpeck, J., Briffa, K. R., Duplessy, J.-C., Joos, F., Masson-Delmotte, V., Olago, D., Otto-Bliesner, B., Peltier, W., Rahmstorf, S., Ramesh, R., Raynaud, D., Rind, D., Solom-

GMDD
7, 3013–3084, 2014

ina, O., Villalba, R., Zhang, D., Trenberth, K. E., Jones, P. D., Ambenje, P., Bojariu, R., Easterling, D., Tank, A. K., Parker, D., Rahimzadeh, F., Renwick, J. A., Rusticucci, M., Soden, B., and Zhai, P.: Palaeoclimate, in: Climate Change 2007: The Physical Science Basis. Contribution of Working Group I to the Fourth Assessment Report of the Intergovernmental Panel on Climate Change, edited by: Solomon, S., Qin, D., Manning, M., Chen, Z., Marquis, M., Averyt, K. B., Tignor, M., and Miller, H. L., Climate Change 2007: The Physical Science Basis. Contribution of Working Group I to the Fourth Assessment Report of the Intergovernmental Panel on Climate Change., chap. 6, Cambridge University Press, Cambridge, UK and New York, NY, USA, 434–497, 2007. 3041, 3044, 3072, 3081

Jungclaus, J. H., Keenlyside, N., Botzet, M., Haak, H., Luo, J.-J., Latif, M., Marotzke, J., Mikolajewicz, U., and Roeckner, E.: Ocean circulation and tropical variability in the coupled model ECHAM5/MPI-OM, J. Climate, 19, 3952–3972, doi:10.1175/JCLI3827.1, 2006. 3021

Jungclaus, J. H., Lorenz, S. J., Timmreck, C., Reick, C. H., Brovkin, V., Six, K., Segschneider, J., Giorgetta, M. A., Crowley, T. J., Pongratz, J., Krivova, N. A., Vieira, L. E., Solanki, S. K., Klocke, D., Botzet, M., Esch, M., Gayler, V., Haak, H., Raddatz, T. J., Roeckner, E., Schnur, R., Widmann, H., Claussen, M., Stevens, B., and Marotzke, J.: Climate and carbon-cycle variability over the last millennium, Clim. Past, 6, 723–737, doi:10.5194/cp-6-723-2010, 2010. 3022

Kang, S. M., Polvani, L. M., Fyfe, J. C., and Sigmond, M.: Impact of polar ozone depletion on subtropical precipitation., Science, 332, 951–4, doi:10.1126/science.1202131, 2011. 3017

Kennedy, J. J., Rayner, N. A., Smith, R. O., Parker, D. E., and Saunby, M.: Reassessing biases and other uncertainties in sea surface temperature observations measured in situ since 1850: 2. Biases and homogenization, J. Geophys. Res., 116, D14104, doi:10.1029/2010JD015220, 2011. 3029

Kirchner, I., Stenchikov, G. L., Graf, H.-F., Robock, A., and Antuña, J. C.: Climate model simulation of winter warming and summer cooling following the 1991 Mount Pinatubo volcanic eruption, J. Geophys. Res., 104, 19039–19055, doi:10.1029/1999JD900213, 1999. 3018

Knutti, R., and Sedláček, J.: Robustness and uncertainties in the new CMIP5 climate model projections, Nat. Clim. Chang., 3, 369–373, doi:10.1038/nclimate1716, 2012. 3047

Kodera, K.: Influence of volcanic eruptions on the troposphere through stratospheric dynamical processes in the Northern Hemisphere winter, J. Geophys. Res., 99, 1273–1282, 1994. 3017

Kodera, K. and Kuroda, Y.: Dynamical response to the solar cycle, J. Geophys. Res., 107, 4749, doi:10.1029/2002JD002224, 2002. 3016, 3017

GMDD
7, 3013–3084, 2014

Kopp, G. and Lean, J. L.: A new, lower value of total solar irradiance: evidence and climate significance, Geophys. Res. Lett., 38, L01706, doi:10.1029/2010GL045777, 2011. 3023
Labitzke, K.: Sunspots, the QBO, and the stratospheric temperature in the north polar region, Geophys. Res. Lett., 14, 535–537, 1987. 3017
Labitzke, K.: Solar variation and stratospheric response, Space Sci. Rev., 125, 247–260, doi:10.1007/s11214-006-9061-6, 2007. 3016, 3017
Lean, J.: Evolution of the sun's spectral irradiance since the Maunder Minimum, Geophys. Res. Lett., 27, 2425–2428, doi:10.1029/2000GL000043, 2000. 3049, 3052
Li, C., Storch, J.-S., and Marotzke, J.: Deep-ocean heat uptake and equilibrium climate response, Clim. Dynam., 40, 1071–1086, doi:10.1007/s00382-012-1350-z, 2012. 3040, 3080
MacFarling-Meure, C.: The natural and anthropogenic variations of carbon dioxide, methane and nitrous oxide during the Holocene from ice core analysis, Ph.D. thesis, University of Melbourne, 2004. 3025
MacFarling-Meure, C., Etheridge, D., Trudinger, C., Steele, P., Langenfelds, R., Van Ommen, T., Smith, A., and Elkins, J.: Law Dome CO_2, CH_4 and N_2O ice core records extended to 2000 years BP, Geophys. Res. Lett., 33, L14810, doi:10.1029/2006GL026152, 2006. 3025
Mann, M. E., Zhang, Z., Rutherford, S., Bradley, R. S., Hughes, M. K., Shindell, D. T., Ammann, C. M., Faluvegi, G., and Ni, F.: Global signatures and dynamical origins of the Little Ice Age and Medieval climate anomaly, Science, 326, 1256–60, doi:10.1126/science.1177303, 2009. 3043, 3044, 3081, 3082
Manzini, E., Giorgetta, M. A., Esch, M., Kornblueh, L., and Roeckner, E.: The influence of sea surface temperatures on the northern winter stratosphere: ensemble simulations with the MAECHAM5 Model, J. Climate, 19, 3863–3881, doi:10.1175/JCLI3826.1, 2006. 3019
Marsland, S.: The Max-Planck-Institute global ocean/sea ice model with orthogonal curvilinear coordinates, Ocean Model., 5, 91–127, doi:10.1016/S1463-5003(02)00015-X, 2003. 3021
Mauritsen, T., Stevens, B., Roeckner, E., Crueger, T., Esch, M., Giorgetta, M., Haak, H., Jungclaus, J., Klocke, D., Matei, D., Mikolajewicz, U., Notz, D., Pincus, R., Schmidt, H., and Tomassini, L.: Tuning the climate of a global model, Journal of Advances in Modeling Earth Systems, 4, M00A01, doi:10.1029/2012MS000154, 2012. 3030, 3031
Maycock, A. C., Shine, K. P., and Joshi, M. M.: The temperature response to stratospheric water vapour changes, Q. J. Roy. Meteor. Soc., 137, 1070–1082, doi:10.1002/qj.822, 2011. 3033

GMDD
7, 3013–3084, 2014

Meehl, G. A., Arblaster, J. M., Branstator, G., and van Loon, H.: A coupled air–sea response mechanism to solar forcing in the pacific region, J. Climate, 21, 2883–2897, doi:10.1175/2007JCLI1776.1, 2008. 3017

Meehl, G. A., Arblaster, J. M., Matthes, K., Sassi, F., and van Loon, H.: Amplifying the pacific climate system response to a small 11-year solar cycle forcings, Science, 325, 1114–1118, doi:10.1126/science.1172872, 2009. 3017

Meraner, K., Mauritsen, T., and Voigt, A.: Robust increase in equilibrium climate sensitivity under global warming, Geophys. Res. Lett., 40, 5944–5948, doi:10.1002/2013GL058118, 2013. 3051

Mignot, J., Khodri, M., Frankignoul, C., and Servonnat, J.: Volcanic impact on the Atlantic Ocean over the last millennium, Clim. Past, 7, 1439–1455, doi:10.5194/cp-7-1439-2011, 2011. 3043

Mlawer, E. J., Taubman, S. J., Brown, P. D., Iaocono, M. J., and Clough, S. A.: Radiative transfer for inhomogeneous atmospheres: RRTM, validated correlated-k model for the longwave, J. Geophys. Res., 102, 663–16 682, 1997. 3019

Muthers, S., Anet, J. G., Raible, C. C., Brönnimann, S., Rozanov, E., Arfeuille, F., Peter, T., Shapiro, A. I., Beer, J., Steinhilber, F., Brugnara, Y., and Schmutz, W.: Northern hemispheric winter warming pattern after tropical volcanic eruptions: sensitivity to the ozone climatology, J. Geophys. Res.-Atmos., 110, 1340–1355, doi:10.1002/2013JD020138, 2014. 3017, 3053

Myhre, G., Shindell, D., Bréon, F.-M., Collins, W., Fuglestvedt, J., Huang, J., Koch, D., Lamarque, J.-F., Lee, D., Mendoza, B., Nakajima, T., Robock, A., Stephens, G., Takemura, T., and Zhang, H.: Anthropogenic and Natural Radiative Forcing, in: Climate change 2013: The physical science basis. Contribution of working group I to the fifth assessment report of the Intergovernmental Panel on Climate Change, edited by: Stocker, T. F., Qin, D., Plattner, G.-K., Tignor, M., Allen, S. K., Boschung, J., Nauels, A., Xia, Y., Bex, V., and Midgley, P., chap. 8, 659–740, Cambridge University Press, Cambridge, UK and New York, NY, USA, 2013. 3049, 3052

Pinto, J. G. and Raible, C. C.: Past and recent changes in the North Atlantic oscillation, Climate Change, 3, 79–90, doi:10.1002/wcc.150, 2012. 3016

Purich, A. and Son, S.-W.: Impact of Antarctic ozone depletion and recovery on Southern Hemisphere precipitation, evaporation, and extreme changes, J. Climate, 25, 3145–3154, doi:10.1175/JCLI-D-11-00383.1, 2012. 3017

Ramaswamy, V., Boucher, O., Haigh, J., Hauglustine, D., Haywood, J., Myhre, G., Nakajima, T., Shi, G. Y., annd Solomon, S.: Radiative forcing of climate change, in: IPCC Third Assessment

GMDD
7, 3013–3084, 2014

Report: Climate Change 2001, edited by: Houghton, J. T., Ding, Y., Griggs, D. J., Noguer, M., van der Linden, P. J., Dai, X., Maskell, K., and Johnson, C. A., 350–416, Cambridge University Press, Cambridge, United Kingdom and New York, NY, USA, 2001. 3049, 3073

Randall, D., Wood, R., Bony, S., Colman, R., Fichefet, T., Fyfe, J., Kattsov, V., Pitman, A., Shukla, J., Stouffer, R., Sumi, A., and Taylor, K.: Climate models and their evaluation, in: Climate Change 2007: The physical science basis, edited by IPCC, 589–660, Cambridge University Press, Cambridge, United Kingdom and New York, NY, USA, 2007. 3040

Rayner, N. A., Parker, D. E., Horton, E. B., Folland, C. K., Alexander, L. V., Rowell, D. P., Kent, E. C., and Kaplan, A.: Global analyses of sea surface temperature, sea ice, and night marine air temperature since the late nineteenth century, J. Geophys. Res., 108, 4407, doi:10.1029/2002JD002670, 2003. 3029

Reichler, T., Kim, J., Manzini, E., and Kröger, J.: A stratospheric connection to Atlantic climate variability, Nat. Geosci., 5, 1–5, doi:10.1038/ngeo1586, 2012. 3015

Roeckner, E., Bäuml, G., Bonaventura, L., Brokopf, R., Esch, M., Giorgetta, M., Hagemann, S., Kirchner, I., Kornblueh, L., Manzini, E., Rhodin, A., Schlese, U., Schulzweida, U., and Tompkins, A.: Report No. 349 the atmospheric general circulation model ECHAM5 – model description, Tech. Rep. 349, Max-Planck Institute for Meteorology, Hamburg, Germany, 2003. 3019

Roeckner, E., Brokopf, R., Esch, M., Giorgetta, M., Hagemann, S., Kornblueh, L., Manzini, E., Schlese, U., and Schulzweida, U.: Sensitivity of simulated climate to horizontal and vertical resolution in the ECHAM5 atmosphere model, J. Climate, 19, 3771–3791, 2006. 3019

Rozanov, E., Schlesinger, M. E., Zubov, V., Yang, F., and Andronova, N. G.: The UIUC three-dimensional stratospheric chemical transport model: description and evaluation of the simulated source gases and ozone, J. Geophys. Res., 104, 11755–11781, doi:10.1029/1999JD900138, 1999. 3019

Rozanov, E., Schlesinger, M. E., and Zubov, V.: The University of Illinois, Urbana-Champaign three-dimensional stratosphere-troposphere general circulation model with interactive ozone photochemistry: fifteen-year control run climatology, J. Geophys. Res., 106, 27233–27254, doi:10.1029/2000JD000058, 2001. 3019

Rozanov, E., Calisto, M., Egorova, T., Peter, T., and Schmutz, W.: Influence of the precipitating energetic particles on atmospheric chemistry and climate, Surv. Geophys., 33, 483–501, doi:10.1007/s10712-012-9192-0, 2012. 3021

GMDD
7, 3013–3084, 2014

Rozanov, E., Schlesinger, M. E., Andronova, N. G., Yang, F., Malyshev, S. L., Zubov, V. A., Egorova, T. A., and Li, B.: Climate/chemistry effects of the Pinatubo volcanic eruption simulated by the UIUC stratosphere/troposphere GCM with interactive photochemistry, J. Geophys. Res., 107, 4594, doi:10.1029/2001JD000974, 2002. 3018

Scaife, A. A., Spangehl, T., Fereday, D. R., Cubasch, U., Langematz, U., Akiyoshi, H., Bekki, S., Braesicke, P., Butchart, N., Chipperfield, M. P., Gettelman, A., Hardiman, S. C., Michou, M., Rozanov, E., and Shepherd, T. G.: Climate change projections and stratosphere–troposphere interaction, Clim. Dynam., 38, 2089–2097, doi:10.1007/s00382-011-1080-7, 2011. 3015

Schmidt, G. A., Jungclaus, J. H., Ammann, C. M., Bard, E., Braconnot, P., Crowley, T. J., Delaygue, G., Joos, F., Krivova, N. A., Muscheler, R., Otto-Bliesner, B. L., Pongratz, J., Shindell, D. T., Solanki, S. K., Steinhilber, F., and Vieira, L. E. A.: Climate forcing reconstructions for use in PMIP simulations of the Last Millennium (v1.1), Geosci. Model Dev., 5, 185–191, doi:10.5194/gmd-5-185-2012, 2012. 3025

Schmidt, H., Rast, S., Bunzel, F., Esch, M., Giorgetta, M., Kinne, S., Krismer, T., Stenchikov, G., Timmreck, C., Tomassini, L., and Walz, M.: Response of the middle atmosphere to anthropogenic and natural forcings in the CMIP5 simulations with the Max Planck Institute Earth system model, Journal of Advances in Modeling Earth Systems, 5, 98–116, doi:10.1002/jame.20014, 2013. 3050

Schraner, M., Rozanov, E., Schnadt Poberaj, C., Kenzelmann, P., Fischer, A. M., Zubov, V., Luo, B. P., Hoyle, C. R., Egorova, T., Fueglistaler, S., Brönnimann, S., Schmutz, W., and Peter, T.: Technical Note: Chemistry-climate model SOCOL: version 2.0 with improved transport and chemistry/microphysics schemes, Atmos. Chem. Phys., 8, 5957–5974, doi:10.5194/acp-8-5957-2008, 2008. 3019

Shapiro, A. I., Schmutz, W., Rozanov, E., Schoell, M., Haberreiter, M., Shapiro, A. V., and Nyeki, S.: A new approach to the long-term reconstruction of the solar irradiance leads to large historical solar forcing, Astron. Astrophys., 529, A67, doi:10.1051/0004-6361/201016173, 2011. 3023, 3025, 3026, 3050, 3052, 3073

Shindell, D. T., Rind, D., Balachandran, N., Lean, J., and Lonergan, P.: Solar cycle variability, ozone, and climate, Science, 284, 305–8, 1999. 3016, 3017

Shindell, D. T., Schmidt, G. A., Mann, M. E., Rind, D., and Waple, A. M.: Solar forcing of regional climate change during the Maunder Minimum, Science, 294, 2149–52, doi:10.1126/science.1064363, 2001. 3017

GMDD
7, 3013–3084, 2014

Shindell, D. T., Schmidt, G. A., Miller, R. L., and Mann, M. E.: Volcanic and solar forcing of climate change during the preindustrial era, J. Climate, 16, 4094–4107, doi:10.1175/1520-0442(2003)016<4094:VASFOC>2.0.CO;2, 2003. 3016

Shindell, D. T., Faluvegi, G., Lacis, A., Hansen, J., and Ruedy, R., and Aguilar, E.: Role of tropospheric ozone increases in 20th-century climate change, J. Geophys. Res., 111, D08302, doi:10.1029/2005JD006348, 2006. 3052

Sigmond, M., Siegmund, P. C., Manzini, E., and Kelder, H.: A simulation of the separate climate effects of middle-atmospheric and tropospheric CO_2 doubling, J. Climate, 17, 2352–2367, 2004. 3015

Smith, T. M., Reynolds, R. W., Peterson, T. C., and Lawrimore, J.: Improvements to NOAA's historical merged land–ocean surface temperature analysis (1880–2006), J. Climate, 21, 2283–2296, doi:10.1175/2007JCLI2100.1, 2008. 3029

Solomon, S., Portmann, R. W., Garcia, R. R., Thomason, L. W., Poole, L. R., Mccormick, M. P., and Cly, C.: The role of aerosol variations in anthropogenic ozone depletion at northern midlatitudes, J. Geophys. Res., 101, 6713–6727, 1996. 3018

Son, S.-W., Gerber, E. P., Perlwitz, J., Polvani, L. M., Gillett, N. P., Seo, K.-H., Eyring, V., Shepherd, T. G., Waugh, D., Akiyoshi, H., Austin, J., Baumgaertner, A., Bekki, S., Braesicke, P., Brühl, C., Butchart, N., Chipperfield, M. P., Cugnet, D., Dameris, M., Dhomse, S., Frith, S., Garny, H., Garcia, R., Hardiman, S. C., Jöckel, P., Lamarque, J. F., Mancini, E., Marchand, M., Michou, M., Nakamura, T., Morgenstern, O., Pitari, G., Plummer, D. A., Pyle, J., Rozanov, E., Scinocca, J. F., Shibata, K., Smale, D., Teyssèdre, H., Tian, W., and Yamashita, Y.: Impact of stratospheric ozone on Southern Hemisphere circulation change: a multimodel assessment, J. Geophys. Res., 115, D00M07, doi:10.1029/2010JD014271, 2010. 3015, 3017

Song, Y. and Robinson, W. A.: Dynamical mechanisms for stratospheric influences on the troposphere, J. Atmos. Sci., 61, 1711–1725, doi:10.1175/1520-0469(2004)061<1711:DMFSIO>2.0.CO;2, 2004. 3016

Staehelin, J., Harris, N. R. P., Appenzeller, C., and Eberhard, J.: Ozone trends: a review, Rev. Geophys., 39, 231–290, doi:10.1029/1999RG000059, 2001. 3047

Steinhilber, F., Abreu, J. A., and Beer, J.: Solar modulation during the Holocene, Astrophys. Space Sci. Trans., 4, 1–6, doi:10.5194/astra-4-1-2008, 2008. 3027

Steinhilber, F., Beer, J., and Fröhlich, C.: Total solar irradiance during the Holocene, Geophys. Res. Lett., 36, 1–5, doi:10.1029/2009GL040142, 2009. 3025

GMDD
7, 3013–3084, 2014

Stenchikov, G., Robock, A., Ramaswamy, V., Schwarzkopf, M. D., Hamilton, K., and Ramachandran, S.: Arctic Oscillation response to the 1991 Mount Pinatubo eruption: effects of volcanic aerosols and ozone depletion, J. Geophys. Res., 107, 1–16, doi:10.1029/2002JD002090, 2002. 3016, 3017, 3018

Stenchikov, G., Hamilton, K., Stouffer, R. J., Robock, A., Ramaswamy, V., Santer, B., and Graf, H.-F.: Arctic Oscillation response to volcanic eruptions in the IPCC AR4 climate models, J. Geophys. Res., 111, 1–17, doi:10.1029/2005JD006286, 2006. 3035

Stenke, A., Hoyle, C. R., Luo, B., Rozanov, E., Gröbner, J., Maag, L., Brönnimann, S., and Peter, T.: Climate and chemistry effects of a regional scale nuclear conflict, Atmos. Chem. Phys., 13, 9713–9729, doi:10.5194/acp-13-9713-2013, 2013a. 3018

Stenke, A., Schraner, M., Rozanov, E., Egorova, T., Luo, B., and Peter, T.: The SOCOL version 3.0 chemistry–climate model: description, evaluation, and implications from an advanced transport algorithm, Geosci. Model Dev., 6, 1407–1427, doi:10.5194/gmd-6-1407-2013, 2013b. 3019, 3031, 3036

Stevenson, D. S., Young, P. J., Naik, V., Lamarque, J.-F., Shindell, D. T., Voulgarakis, A., Skeie, R. B., Dalsoren, S. B., Myhre, G., Berntsen, T. K., Folberth, G. A., Rumbold, S. T., Collins, W. J., MacKenzie, I. A., Doherty, R. M., Zeng, G., van Noije, T. P. C., Strunk, A., Bergmann, D., Cameron-Smith, P., Plummer, D. A., Strode, S. A., Horowitz, L., Lee, Y. H., Szopa, S., Sudo, K., Nagashima, T., Josse, B., Cionni, I., Righi, M., Eyring, V., Conley, A., Bowman, K. W., Wild, O., and Archibald, A.: Tropospheric ozone changes, radiative forcing and attribution to emissions in the Atmospheric Chemistry and Climate Model Intercomparison Project (ACCMIP), Atmos. Chem. Phys., 13, 3063–3085, doi:10.5194/acp-13-3063-2013, 2013. 3047, 3052

Stocker, T., Qin, D., Plattner, G.-K., Alexander, L., Allen, S., Bindoff, N., Bréon, F.-M., Church, J., Cubasch, U., Emori, S., Forster, P., Friedlingstein, P., Gillett, N., Gregory, J., Hartmann, D., Jansen, E., Kirtman, B., Knutti, R., Kumar, K. K., Lemke, P., Marotzke, J., Masson-Delmotte, V., Meehl, G., Mokhov, I., Piao, S., Ramaswamy, V., Randall, D., Rhein, M., Rojas, M., Sabine, C., Shindell, D., Talley, L., Vaughan, D., and Xie, S.-P.: Technical Summary, in: Climate change 2013: the Physical Science Basis. Contribution of working group I to the fifth assessment report of the Intergovernmental Panel on Climate Change, edited by: Stocker, T., Qin, D., Plattner, G.-K., Tignor, M., Allen, S., Boschung, J., Nauels, A., Xia, Y., Bex, V., and Midgley, P., 33–115, Cambridge University Press, Cambridge, UK and New York, NY, USA, 2013. 3040

GMDD
7, 3013–3084, 2014

Thompson, D. W. and Wallace, J. M.: Regional climate impacts of the Northern Hemisphere annular mode, Science, 293, 85–9, doi:10.1126/science.1058958, 2001. 3035
Thompson, D. W. J., Baldwin, M. P., and Solomon, S.: Stratosphere-troposphere coupling in the Southern Hemisphere, J. Atmos. Sci., 62, 708–715, 2005. 3015, 3016
Thompson, D. W. J., Furtado, J. C., and Shepherd, T. G.: On the tropospheric response to anomalous stratospheric wave drag and radiative heating, J. Atmos. Sci., 63, 2616–2629, 2006. 3016
Thompson, D. W. J., Solomon, S., Kushner, P. J., England, M. H., Grise, K. M., and Karoly, D. J.: Signatures of the Antarctic ozone hole in Southern Hemisphere surface climate change, Nat. Geosci., 4, 741–749, doi:10.1038/ngeo1296, 2011. 3015, 3017
Tie, X. and Brasseur, G.: The response of stratospheric ozone to volcanic eruptions: sensitivity to atmospheric chlorine loading, Geophys. Res. Lett., 22, 3035–3038, 1995. 3018
Uppala, S. M., Kållberg, P. W., Simmons, A. J., Andrae, U., Bechtold, V. D. C., Fiorino, M., Gibson, J. K., Haseler, J., Hernandez, A., Kelly, G. A., Li, X., Onogi, K., Saarinen, S., Sokka, N., Allan, R. P., Andersson, E., Arpe, K., Balmaseda, M. A., Beljaars, A. C. M., Berg, L. V. D., Bidlot, J., Bormann, N., Caires, S., Chevallier, F., Dethof, A., Dragosavac, M., Fisher, M., Fuentes, M., Hagemann, S., Hólm, E., Hoskins, B. J., Isaksen, L., Janssen, P. A. E. M., Jenne, R., Mcnally, A. P., Mahfouf, J.-F., Morcrette, J.-J., Rayner, N. A., Saunders, R. W., Simon, P., Sterl, A., Trenberth, K. E., Untch, A., Vasiljevic, D., Viterbo, P., and Woollen, J.: The ERA-40 re-analysis, Q. J. Roy. Meteor. Soc., 131, 2961–3012, doi:10.1256/qj.04.176, 2005. 3029, 3070
Valcke, S.: The OASIS3 coupler: a European climate modelling community software, Geosci. Model Dev., 6, 373–388, doi:10.5194/gmd-6-373-2013, 2013. 3022
Varma, V., Prange, M., Spangehl, T., Lamy, F., Cubasch, U., and Schulz, M.: Impact of solar-induced stratospheric ozone decline on Southern Hemisphere westerlies during the Late Maunder Minimum, Geophys. Res. Lett., 39, L20704, doi:10.1029/2012GL053403, 2012. 3017
Wang, Y., Lean, J. L., and Sheeley Jr., N. R.: Modeling the sun's magnetic field and irradiance since 1713, Astrophys. J., 625, 522–538, doi:10.1086/429689, 2005. 3049, 3052
Wanner, H., Brönnimann, S., Casty, C., Gyalistras, D., Luterbacher, J., Schmutz, C., and Stephenson, D. B., and Xoplaki, E.: North Atlantic Oscillation – concepts and studies, Surv. Geophys., 22, 321–381, doi:10.1023/A:1014217317898, 2001. 3016

GMDD
7, 3013–3084, 2014

Waugh, D. W., Oman, L., Newman, P. A., Stolarski, R. S., Pawson, S., Nielsen, J. E., and Perlwitz, J.: Effect of zonal asymmetries in stratospheric ozone on simulated Southern Hemisphere climate trends, Geophys. Res. Lett., 36, L18701, doi:10.1029/2009GL040419, 2009. 3021

Weisenstein, D., Yue, G., Ko, M., Sze, N., Rodriguez, J., and Scott, C.: A two-dimensional model of sulfur species and aerosols, J. Geophys. Res., 102, 13019–13035, 1997. 3027

Woollings, T., Charlton-Perez, A., Ineson, S., Marshall, A. G., and Masato, G.: Associations between stratospheric variability and tropospheric blocking, J. Geophys. Res., 115, D06108, doi:10.1029/2009JD012742, 2010. 3035

GMDD
7, 3013–3084, 2014

Table 1. Overview of the experiments used in this study. In column "chem" the usage of the interactive chemistry module is indicates. Column "type" denotes whether the experiment is performed as time-slice (t-slice) experiment with invariant boundary conditions or as transient (trans) simulation with time varying boundary conditions.

	length/period	chemistry	solar amplitude	type	forcings
CHEM	1400 yr	yes	const.	t-slice	const. 1600 AD
NOCHEM	222 yr	no	const.	t-slice	const. 1600 AD
2xCO2	70 yr	yes	const.	t-slice	const. 1990, expect for CO_2
2xCO2_NC	70 yr	no	const.	t-slice	const. 1990, expect for CO_2
4xCO2	150 yr	yes	const.	t-slice	const. 1990, expect for CO_2
M1	1600–2000	yes	medium	trans.	all
M2	1600–2000	yes	medium	trans.	all
L1	1600–2000	yes	large	trans.	all
L2	1600–2000	yes	large	trans.	all
SOLAR	1840–2000	no	medium	trans.	solar only
GHG	1840–2000	no	const.	trans.	GHG only
AERO	1840–2000	no	const.	trans.	aerosols only
OZONE	1840–2000	no	const.	trans.	ozone only
FULL	1840–2000	no	medium	trans.	all

GMDD
7, 3013–3084, 2014

Table 2. Climatological indices for the winter (DJF) zonal wind component at 50 hPa in different latitudes, similar to Driscoll et al. (2012). Climatological indices for CHEM and NOCHEM are calculated over the common 222 year period. Reanalysis values are based on ERA Interim for the period 1979–2013 (Dee et al., 2011) and ERA 40 for the years 1957–2002 (Uppala et al., 2005). Values given denote the average zonal wind speed in the given latitude range at 50 hPa in $m\,s^{-1}$; the standard deviation is given in brackets.

	30° S–30° N	55–65° N
CHEM	−2.4 (3.6)	23.1 (7.7)
NOCHEM	−2.4 (3.5)	22.5 (7.8)
ERA Interim	−3.7 (5.1)	19.0 (8.6)
ERA 40	−3.8 (5.1)	19.1 (8.1)

GMDD
7, 3013–3084, 2014

Table 3. Average number of SSW events per winter (NDJFM) following the definition of Charlton and Polvani (2007). SSW events for CHEM and NOCHEM are calculated over the common 222 year period. For comparison the reanalysis products ERA 40 (1957–2002) and ERA Interim (1979–2013) are used.

	Nov	Dec	Jan	Feb	Mar	$\sum$
CHEM	0.12	0.07	0.07	0.14	0.23	0.63
NOCHEM	0.10	0.07	0.10	0.19	0.21	0.67
ERA40	0.02	0.09	0.24	0.16	0.13	0.64
ERA Interim	0.00	0.12	0.18	0.26	0.21	0.76

GMDD
7, 3013–3084, 2014

Table 4. NH temperature differences [K] for the late Maunder Minimum (1679–1699) relative to the two reference periods 1600–1629 and 1770–1799 and for the Dalton Minimum (1800–1829) relative to the period 1770–1799. "Reconstructions" refers to the temperature anomaly of the median of the reconstructed NH temperature anomalies in Jansen et al. (2007).

	1670/1699 – 1600/1629	1670/1699 – 1770/1799	1800/1829 – 1770/1799
M1	−0.24	−0.48	−0.15
M2	−0.03	−0.35	−0.30
L1	−0.34	−0.54	−0.18
L2	−0.40	−0.36	−0.13
reconstructions	0.03	−0.15	−0.08

GMDD
7, 3013–3084, 2014

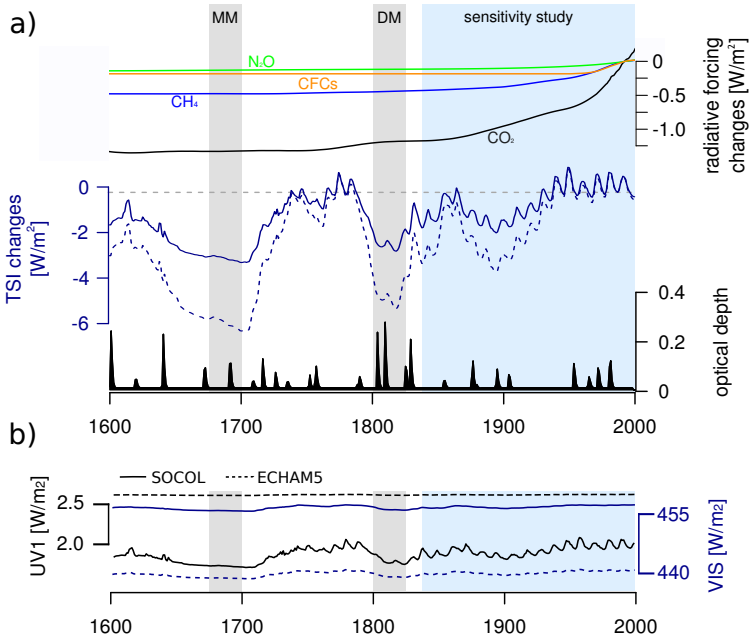

Fig. 1. (a) Overview of the major external forcings applied in the transient simulations. Top: Evolution of the radiative forcing from major greenhouse gases CO_2, CH_4, N_2O, and CFCs (calculated as in Ramaswamy et al., 2001). For CFCs the sum of CFC-11 and CFC-22 is shown as representative forcing. Values are expressed as deviations of the radiative forcing from the 1990 value. Middle: Total solar irradiance with respect to 1990. The dashed line represents the mean value of the TSI reconstruction of Shapiro et al. (2011), the solid line follows the upper envelope of the uncertainty range. Bottom: Volcanic forcing as global mean, annual mean aerosol optical depth in the visible band (Arfeuille et al., 2014). Three periods are highlighted: MM: late Maunder Minimum (1670–1699); DM: Dalton Minimum (1800–1829); and the period used in the sensitivity simulations (1840–2000). **(b)** Variability in the UV1 (185–250 nm) and visible (440–690 nm) spectral band (solid) in the SSI reconstruction of Shapiro et al. (2011) and (dashed) in ECHAM5 when the same TSI is applied.

GMDD
7, 3013–3084, 2014
SOCOL-MPIOM
S. Muthers et al.

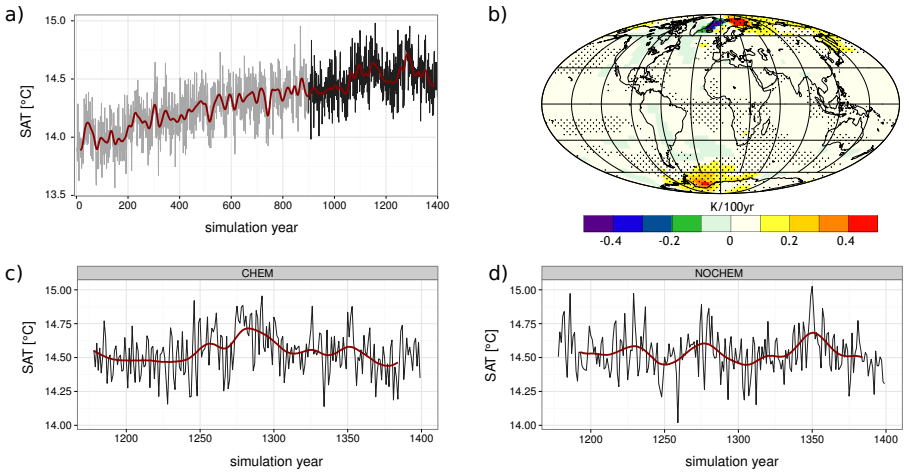

Fig. 2. (a) Time series of the global mean 2 m air temperature as annual mean values (black) and 31 year low pass filtered values (red) for the simulation with interactive chemistry (CHEM). The spin-up period is indicated by light grey colours, the last 500 years, which are used to calculate the trend pattern **(b)**, are shown in black colours. **(b)** Linear temperature trends in K/100 yr for the last 500 years in CHEM. Regions with significant trends are stippled. **(c, d)** Time series of the global mean 2 m air temperature as annual mean values (black) and 31 year low pass filtered values (red) for the simulation with (CHEM) and without (NOCHEM) interactive chemistry over the common 222 year period.

GMDD
7, 3013–3084, 2014

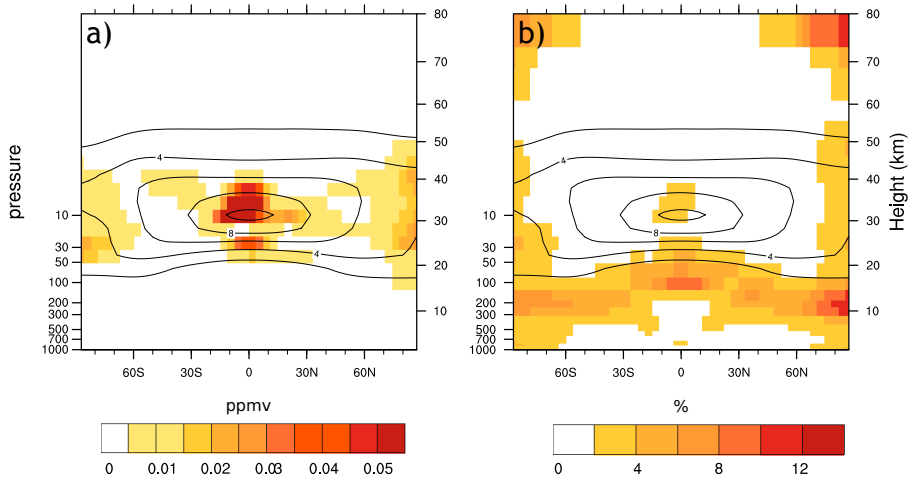

Fig. 3. Variability in the annual mean zonally averaged ozone mixing ratios in the CHEM simulation. **(a)** Standard deviation (in ppmv). **(b)** Variability expressed as standard deviation normalized by the long-term mean (given as percentages). Contours show the long term-mean ozone concentrations.

GMDD
7, 3013–3084, 2014

a) temperature differences

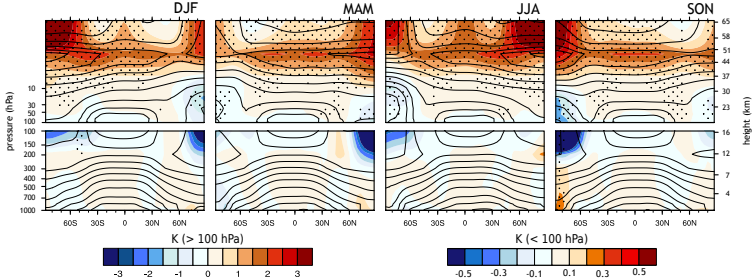

b) zonal wind differences

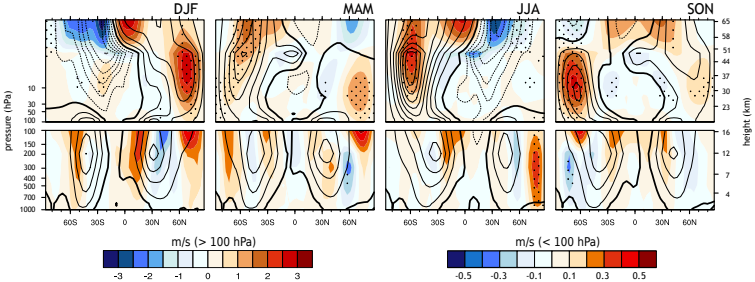

c) variance ratios

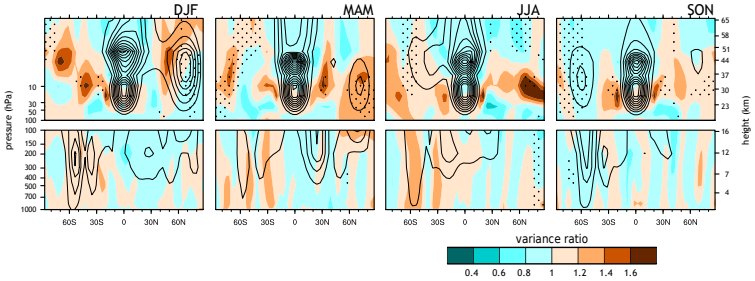

GMDD
7, 3013–3084, 2014

Fig. 4. Zonal and seasonal mean anomalies between CHEM and NOCHEM, i.e., CHEM minus NOCHEM for **(a)** temperatures, **(b)** the zonal wind component, and **(c)** the variance ratio of the zonal mean wind component between CHEM and NOCHEM, i.e., *variance(CHEM)/variance(NOCHEM)*. Atmospheric levels above (top) and below (bottom) 100 hPa are displayed separately to improve readability in the lower atmosphere. Contours: seasonal means in CHEM with contours **(a)** from 230 K to 300 K by 10 K and **(b)** $-50\,\mathrm{m\,s^{-1}}$ to $50\,\mathrm{m\,s^{-1}}$ by $10\,\mathrm{m\,s^{-1}}$. In **(c)** the average seasonal variance in CHEM is shown, with contours from $0\,\mathrm{m^2\,s^{-2}}$ to $140\,\mathrm{m^2\,s^{-2}}$ by $25\,\mathrm{m^2\,s^{-2}}$ for levels above 100 hPa and $0\,\mathrm{m^2\,s^{-2}}$ to $15\,\mathrm{m^2\,s^{-2}}$ by $3\,\mathrm{m^2\,s^{-2}}$ for levels below 100 hPa. Stippling: significant differences between the ensembles. In case of the seasonal mean comparison **(a, b)** a Student's *t* test is used. The variance comparison is based on a F-Test. Test results with $p \leq 0.05$ are stippled. Differences are calculated over the common 222 year period.

GMDD
7, 3013–3084, 2014

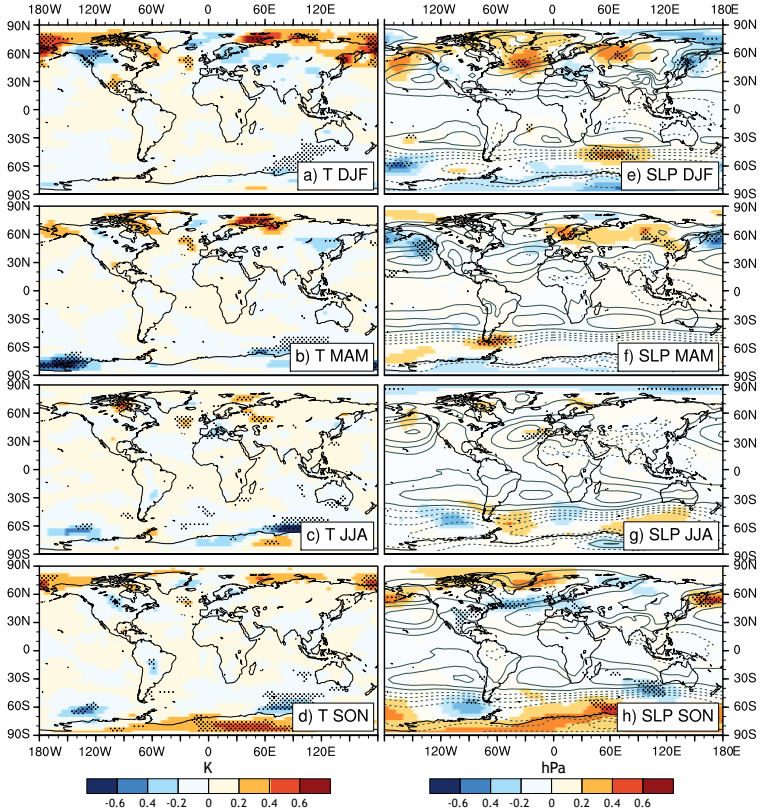

Fig. 5. Differences in the seasonal mean 2 m temperature (left) and sea level pressure (right) between the CHEM and NOCHEM control simulation. Seasons are displayed from top to bottom (DJF: **a**, **e**; MAM: **b**, **f**; JJA: **c**, **g**; SON: **d**, **h**). Gray contours in the sea level pressure panels display the seasonal average field in CHEM. The significance of the anomalies is indicated by stipplings for $p \leq 0.05$ (Student's t test).

GMDD
7, 3013–3084, 2014

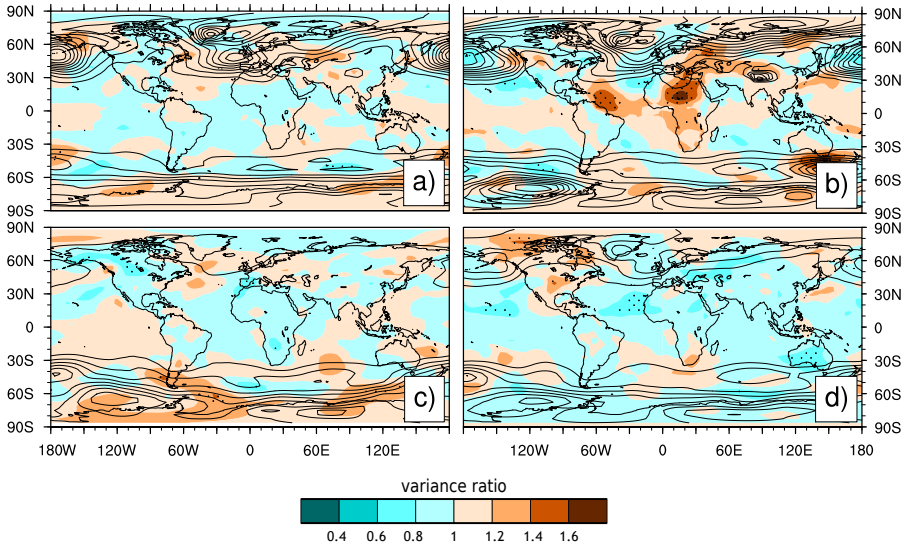

Fig. 6. Variance ratio (i.e. *variance(CHEM)/variance(NOCHEM)*) for the seasonal mean sea level pressure with **(a)** DJF, **(b)** MAM, **(c)** JJA, and **(d)** SON. Stippling: significant differences between the ensembles based on a F Test. Test results with $p \leq 0.05$ are stippled. Contours: seasonal variance in CHEM. Differences are calculated over the common 222 year period.

GMDD
7, 3013–3084, 2014

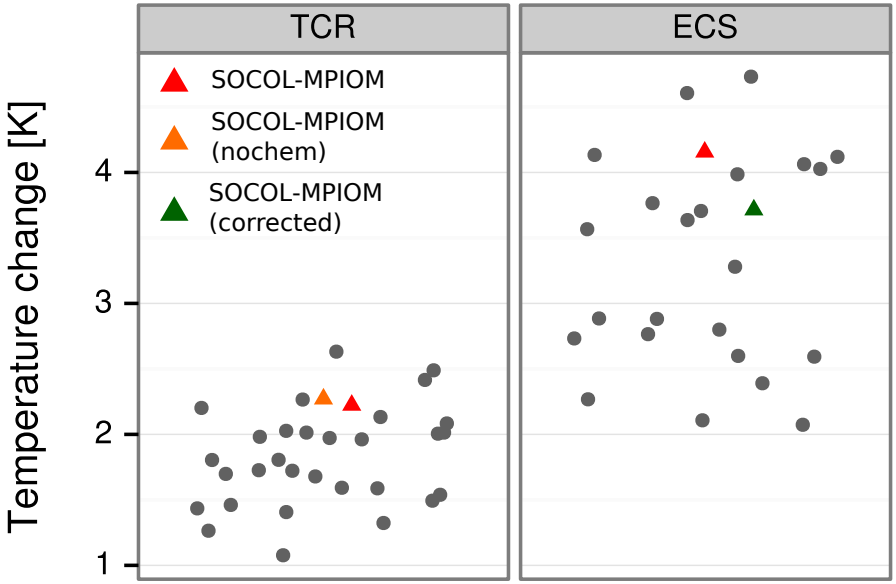

Fig. 7. Comparison of the Transient Climate Response (TCR, left) and the Equilibrium Climate Sensitivity (ECS, right) for a doubling of CO_2 for the CMIP5 (grey dots, Flato et al., 2013) and SOCOL-MPIOM (triangles). The ECS is determined by two different approaches. The first estimate (red triangle) considers only the top-of-the-atmosphere (TOA) radiative flux and the global mean temperature (Gregory et al., 2004). For the seconds estimate (green triangle), the first estimate is corrected by the deep ocean heat uptake, following Li et al. (2012).

GMDD
7, 3013–3084, 2014

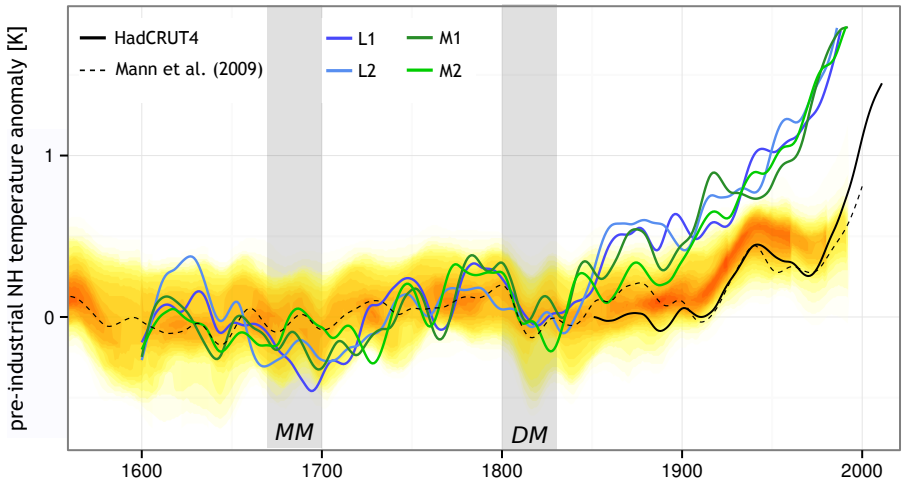

Fig. 8. NH average 2 m temperatures for the four transient simulations (coloured lines) in comparison to the probability range (yellow/ref shading) of different NH temperature reconstructions (Jansen et al., 2007). The ensemble members L1 and L2 correspond to the large amplitude solar forcing, M1 and M1 were forced by the moderate TSI amplitude. Furthermore, the NH averaged pre-industrial temperature anomaly in the Mann et al. (2009) reconstruction, which is used for the spatial comparison, and in HadCRUT4 is shown. Reconstructions and simulations are given as anomalies to the pre-industrial period 1600–1850. This allows for a direct comparison of the variability in the pre-industrial period despite the strong temperature trend from 1850 on. HadCRUT4 values are displayed relative to the value for the year 1850. All time series are decadally smoothed with a cubic-smoothing spline. Grey bars indicate the 30 yr periods covering the MM and the DM, which are used to calculate the temperature anomalies.

GMDD
7, 3013–3084, 2014
SOCOL-MPIOM
S. Muthers et al.

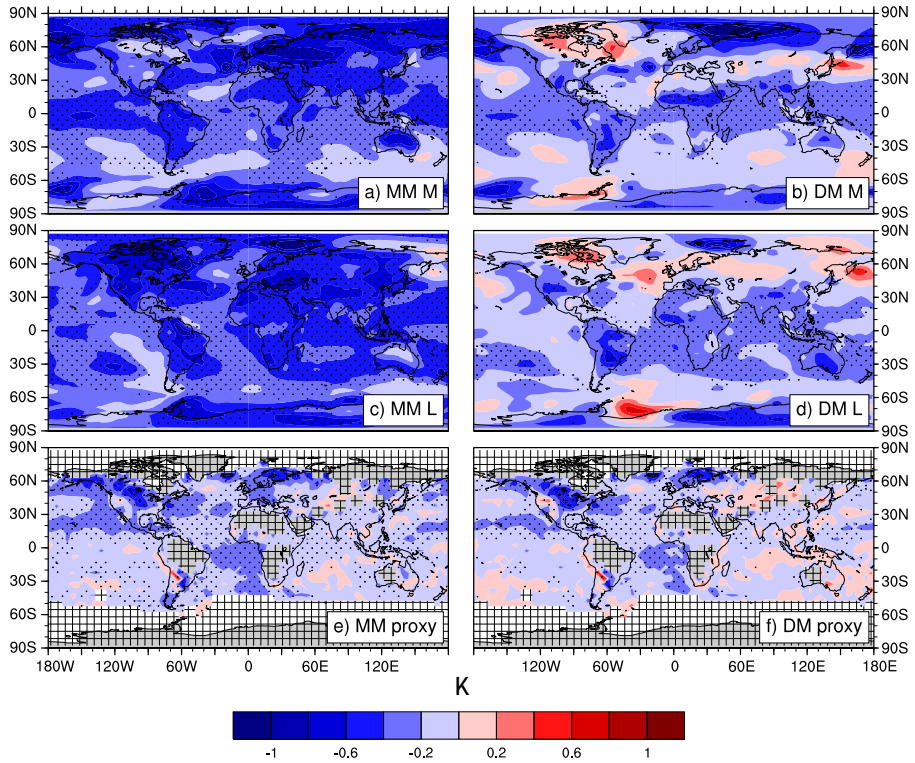

Fig. 9. Temperature differences for the Maunder Minimum (1670–1699, left, **a**, **c**, **e**) and the Dalton Minimum (1800–1829, right, **b**, **d**, **f**) with respect to the common reference period (1770–1799) for the ensemble average with medium solar amplitude (top, **a**, **c**), large solar amplitude (middle, **b**, **d**) and the spatial reconstruction of Mann et al. (2009) (bottom, **e**, **f**). Stippling: significant differences (Student's t test, $p \leq 0.05$).

GMDD
7, 3013–3084, 2014

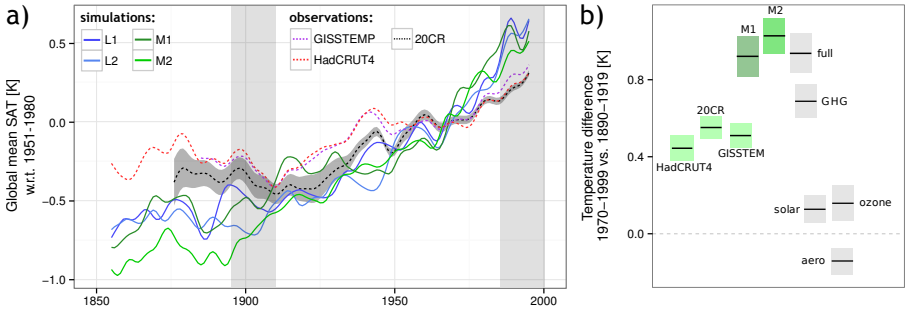

Fig. 10. (a) Global mean, annually averaged surface air temperature in the transient simulations and different observation based data sets. All time series are filtered by an 11 year low pass filter. For 20CR the ensemble spread (ensemble standard deviation) is indicated by the shaded area. All data sets are given as anomalies w.r.t. the period 1951–1980. **(b)** Average global mean temperature increase for the period 1970–1999 relative to 1890–1919 (highlighted by the grey regions in **a**). M1 and M2 refer to the two transient simulations with medium solar forcing amplitude. Bars indicate the average temperature difference between the two periods, gray boxes represent the 95 % confidence intervals.

GMDD
7, 3013–3084, 2014
SOCOL-MPIOM
S. Muthers et al.

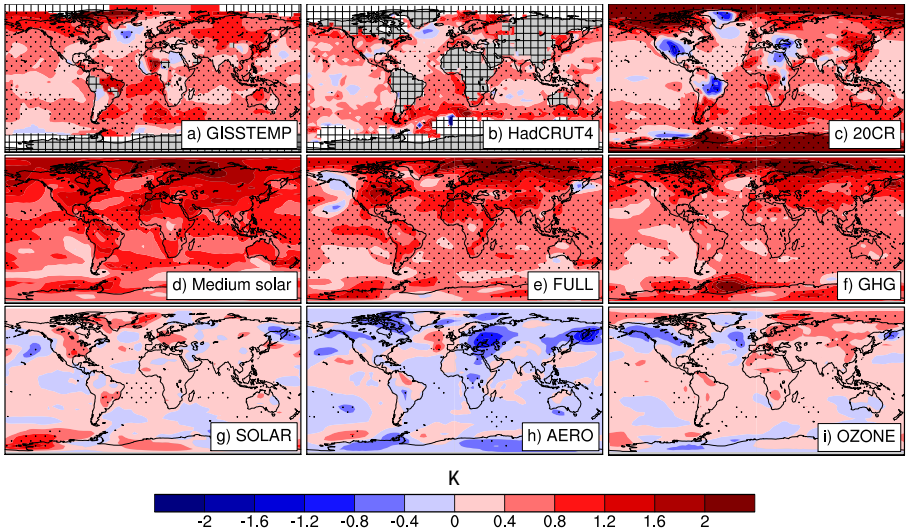

Fig. 11. Surface air temperature difference [K] between the two 30 yr periods 1890–1919 and 1970–1999 for different data sets and simulations. Top: observational data sets **(a)** GISSTEMP, **(b)** HadCRUT4, **(c)** 20CR. Middle and bottom: model experiments **(d)** medium solar – ensemble average **(e)** full forcing sensitivity run, **(f)** GHG only, **(g)** solar only, **(h)** aerosols only, and **(i)** ozone only. Stippling: significant differences using a Students t test ($p \leq 0.05$) and taking auto-correlation into account. For **(a)** GISSTEMP and **(b)** HadCRUT4 missing values are indicated by the cross pattern.

GMDD
7, 3013–3084, 2014